L

Extension of the Pressure Time Method to 3-Dimensional Flows

Mehrdad Kalantar Neyestanaki

Fluid Mechanics

LULEÅ
UNIVERSITY
OF TECHNOLOGY
L

Extension of the Pressure Time Method to 3-Dimensional Flows

By

Mehrdad Kalantar Neyestanaki

Division of Fluid and Experimental Mechanics
Department of Engineering Sciences and Mathematics
Luleå University of Technology
SE-971 87 Luleå
Sweden
Luleå, Feb 2024

Abstract

Hydropower has stood as a clean and sustainable energy source since the late 19th century. Many turbines were built 50 to 70 years ago and require refurbishment. It is important to assess the efficiency of turbines before and after refurbishment to meet performance guarantees. However, the flow rate makes such estimation challenging. Moreover, determining the volumetric flow rate is crucial to specify the hydraulic performance characteristics of hydraulic turbines. The pressure-time method allows measuring the flow rate in hydraulic turbines, according to the IEC 60041 standard, based on transforming momentum into pressure during the deceleration of a liquid mass. The flow rate is obtained by integrating the differential pressure and the pressure loss history between two cross-sections.

This method assumes a one-dimensional flow (1D) and is limited to straight pipes with a uniform cross-section and specific restrictions on length (L>10 m), velocity (U.L>50 m^2s^{-1}) and distance between the measurement sections from any irregularities in the pipeline. However, challenges arise when applying this method in low-head hydropower plants due to the short lengths, irregularities like bends, variation in cross section and developing flows in the intake. This thesis aims to improve the performance of the method out of IEC standards for conditions similar to low-head conditions.

The thesis is divided into the numerical simulation of the fluid during the pressure-time method transient, experimental measurement, and a combination of both. The physics in the pressure-time method is studied to compare different assumptions to estimate the viscous losses for both developed and developing flow. Moreover, a test rig has been developed to extend the method's applicability. The test rig is designed to study the pressure-time method for developing flow conditions, small measurement lengths, variable cross-section and the presence of bend close to measurement sections, which could be similar to low-head turbine conditions.

Finally, the data are evaluated using the new approach combining the 1D pressure-time method and three-dimensional computational fluid dynamics (3D CFD).

Acknowledgements

I dedicate this thesis to you. Looking back on my PhD journey, I recognize the priceless role you played in both my personal and academic growth. From you, I learned the art of resilience and perseverance, and without you, the inception and completion of this doctoral pursuit would not have been possible. Through you, I discovered facets of myself I never knew existed.

To my parents, Fatemeh and Mohammadreza, and my sister, Mehrnoush, I am certain that you take pride in my achievements and the journey I have undertaken. Although the intricacies of my research may not be within your realm of expertise, your boundless love, support, and unwavering dedication have been the cornerstone of my success. Expressing my gratitude in words feels inadequate, yet I am endlessly blessed to have you in my life.

I would like to express my heartfelt gratitude to my family in Sweden—Jafar, Maryam, Hafez, Armin, Zahra, Ava and Babak. Your precious support and presence during moments of despair have been a source of immeasurable comfort and strength. Thank you for always being there for me.

Finally, I commend myself for the dedication and commitment I demonstrated throughout this journey. While it meant sacrificing weekends and holidays, I am grateful for the steadfastness I exhibited.

Feb. 2024, Luleå

Mehrdad Kalantar Neyestanaki

Thesis

The doctoral thesis includes a summary of the research work done during the Ph.D. study, and related peer-reviewed journal articles.

Paper A   Neyestanaki, M.K.; Dunca, G.; Jonsson, P.; Cervantes, M.J., Numerical Investigation of the Pressure-Time Method, Head loss in Developed and Developing Flows, International Journal of Fluid Machinery and Systems, volume. 16 (4) (2023) 332–345.

https://www.jstage.jst.go.jp/article/ijfms/16/4/16_332/_article/-char/ja

Paper B   Neyestanaki, M.K.; Dunca, G.; Jonsson, P.; Cervantes, M.J., A Comparison of Different Methods for Modelling Water Hammer Valve Closure with CFD. Water 2023, Vol. 15, Page 1510 2023, 15, 1510, doi:10.3390/W15081510

https://www.mdpi.com/2073-4441/15/8/1510

Paper C   Neyestanaki, M.K.; Dunca, G.; Jonsson, P.; Cervantes, M.J., Experimental Study of The Pressure-Time Method With Potential Application for Low-Head Hydropower. J Fluids Eng 2023, 145, 1–45, doi:10.1115/1.4062090.

https://doi.org/10.1115/1.4062090

Paper D   Neyestanaki, M.K.; Dunca, G.; Jonsson, P.; Cervantes, M.J., Extending of The Pressure-Time Method by CFD Simulation for Pipe With Variable Cross-Section , J. Fluid Eng. (2024) 146

https://doi.org/10.1115/1.4063491

Paper E   Neyestanaki, M.K.; Dunca, G.; Jonsson, P.; Cervantes, M.J., Extending The Pressure-Time Method to Bend Using 3D-CFD , Flow Measurement and Instrumentation 2024

https://doi.org/10.1016/j.flowmeasinst.2024.102535

Contents of the Thesis

Publication…………………………. ....

Paper A: Numerical Investigation of the Pressure-Time Method, Head loss in Developed and Developing Flows

Paper B: A Comparison of Different Methods for Modelling Water Hammer Valve Closure with CFD.

Paper C: Experimental Study of The Pressure-Time Method With Potential Application for Low-Head Hydropower.

Paper D: Extending of The Pressure-Time Method by CFD Simulation for Pipe With Variable Cross-Section

Paper E: Extending The Pressure-Time Method to Bend Using 3D-CFD

List of Tables

List of Figures

Figure 26 Variation of the dynamic pressure between sections HD - HE using a constant value for the kinetic energy correction factor and a value predicted by 3D CFD.

Figure 27 Variation of the pressure loss due to friction between sections HD - HE based on a constant friction factor and as predicted by 3D CFD (axial (z-axis) and magnitude of total wall shear stress)

Figure 28   Variation of the deviation compared to the reference flow meter function of endpoints for the 1D pressure-time method for a constant value of α and 3D CFD for two iterations

Figure 29 Improvement of flow rate deviation compared to the reference flow meter after applying the methodology for 3 cases at a) higher deviation bound, b) mean and c) lower deviation bound.

Figure 30 Experimental and 3D CFD numerical differential pressure between section HA-HB at the location of the pressure taps

Figure 31 Pressure distribution and surface streamlines at different sections after the bend from steady-state simulation

Figure 32 Normalised pressure measurement deviation at four sections

Figure 33 Flowrate deviation compared to the reference flow meter function of endpoint for all cases (a) HA-HB, (b) VA-HA, (c) HB-HC, (d) HA-HC, (e) VH-HB

Figure 34 Flowrate deviation for all cases; × represents the mean deviation of the experimental measurement with 1D pressure-time method, ⌑ represents the mean deviation with 3D CFD methodology. The bars represent the uncertainty with 95 % confidence interval based on the standard pressure-time method.

Figure 35   The concentric reducer geometry used for derivation of the equations

Nomenclature

A	Area [m^2]
b_r	Systematic uncertainty [-]
C	The geometry factor [m^{-1}]
CF	Friction correction factor [-]
D	Pipe diameter [m]
e_{Var}	Uncertainty of variable [-]
$\bar{E}$	Mean error/deviation compared to the reference flow meter [%]
q_s	Quasi-steady friction factor [-]
K_z	Accuracy class [-]
K	Constant coefficient of friction losses [-]
L	Pipe length [m]
N	Number of measurements [-]
p	Average pressure at section [Pa]
p_{tap}	Measured pressure at pressure tap [Pa]
ΔP	Differential pressure [Pa]
ΔP_d	Dynamic pressure variation [Pa]
ΔP_f	Pressure loss due to friction [Pa]
q	Leakage flow rate [m^3 s^{-1}]
Q	Flow rate [m^3 s^{-1}]
Re	Reynolds number [-]
S_r	Random uncertainty [-]
t	Time [s]
t_f	Upper time-limit of integration of free pressure oscillation signal [s]
U	Cross-sectional velocity [m s^{-1}]
u_i	Fluctuating velocity [m s^{-1}]
$U_{\tau 0}$	Friction velocity at the initial steady condition [m s^{-1}]
x_i	Coordinate [m]

y^+ Dimensionless wall distance [-]

Greek Letters

α Kinetic energy coefficient [-]

μ Dynamic viscosity [Kg m^{-1} s^{-1}]

ρ Density [kgm^{-3}]

δ Relative uncertainty [-]

ε Residual [-]

σ_r Random uncertainty [-]

τ Wall shear stress [Pa]

Δ Differences [-]

Subscripts

c Cross-section

R Reducer

Con Constant

EFM Electromagnetic flowmeter

Var Variable

t_0 Initial time before valve movement in the steady-state condition

QS Quasi-steady

1. Introduction

1.1. Hydropower

Hydropower, a clean and sustainable energy source, the development of which started in the late 19th century, has been and continues to be used extensively to generate electricity. Based on the Renewable Energy Report (2019), the global contribution of hydropower electricity is 17% of the world's electricity production, the third-largest source of energy after coal and natural gas [1]. As reported by Nordic Energy Research, renewable resources account for approximately 59% of Sweden's electricity production, with hydropower, at close to 40%, providing the largest contribution within this category [2]. The Swedish hydropower plants mainly use low-head machines, with most below 200 m head.

Moreover, hydropower provides an effective means for regulating fluctuations in the electrical grid due to its ability to adjust its load rapidly. Hence, hydropower has a significant role to play in renewable-energy power production.

Hydraulic turbines are used in hydropower plants to efficiently convert water's potential energy into electrical energy, with a hydraulic efficiency rate exceeding 95%. Figure 1 shows a schematic representation of the operating principle of a hydropower plant [3]. Water enters from the reservoir and follows a path through the penstock. As the water flows through, it imparts rotational motion to the runner, enabling electricity generation by the connected generator.
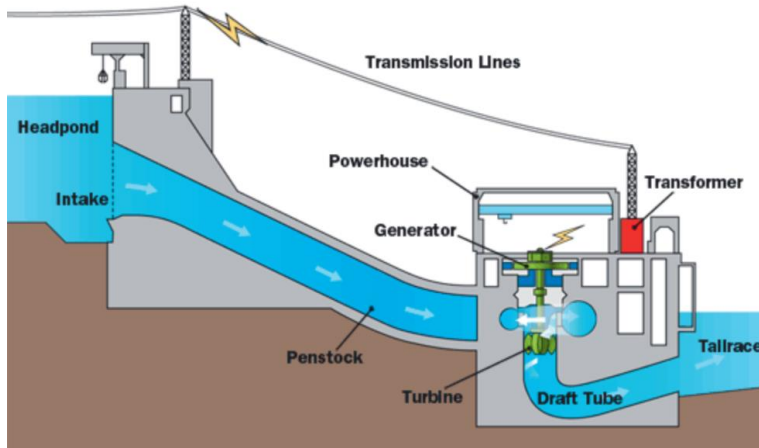
Figure 1 The schematic of a hydropower plant [3]

1.2. Flow measurement

A significant number of turbines were built 50 to 70 years ago. Thus, many hydropower facilities now require refurbishment, and comparing the efficiency of these refurbishments before and after is essential for guarantee fulfilment and operational optimisation. Different techniques can be used to assess the hydraulic turbine's efficiency; the measurement procedures include direct (thermodynamic approach with limitation for low-head condition) and indirect (head and flow rate estimation) approaches [3].

IEC-60041 recommends multiple methods for discharge measurement and Table 1 lists discharge measurement methods, estimated costs, and development status specifically in respect of low-head plants with heads less than 50 m [4] (2012). The drawbacks of Current meters include higher costs, longer installation pauses, and limitations such as changes in flow angles caused by variable intake cross-sections. While potentially valuable, model testing can be prohibitively expensive, with estimated costs reaching approximately 5 million SEK for the manufacture of a scale model. The Winter-Kennedy method stands out as Sweden's most commonly used approach for discharge measurement [4]. If pressure sensors are already installed, it benefits from low cost and short downtimes. However, it is crucial to remember that the Winter-Kennedy approach requires calibration and is a relative method.

In contrast, the pressure-time method is an affordable absolute method for discharge measurement. If pressure taps are already in place and cross-sections have been measured, the cost of implementing the pressure-time method is approximately 200 kSEK. Therefore,

the pressure-time method can be used as an inexpensive absolute method for calibrating the Winter-Kennedy method.

Table 1 Available discharge measurement methods and their development statuses for low-head plants [4]

Method	Type	Development status for low head	Estimated cost (MSEK)	Uncertainty at 95% confidence
Winter-Kennedy	Relative	Low	0.2	$< \pm 10\%$
Pressure-time	Absolute	Very low	0.2	$< \pm 1.4\%$
Transit time	Absolute	Average	1	$< \pm 0.1\%$
Scintillation	Absolute	Low	1	$< \pm 0.5\%$
Current meter	Absolute	Very good	1	$< \pm 1.2\%$
Dilution	Absolute	Very low	0.2	$< \pm 3\%$
Volumetric	Absolute	Very low	0.2	$< \pm 1.2\%$
Model testing	Absolute	Very good	5	$< \pm 0.2\%$

Summarising briefly, the combination of the Winter-Kennedy and pressure-time methods seems appealing for discharge measurement, however, application of the pressure-time method to shorter penstocks is currently limited because of a lack of understanding and experience in such scenarios.

1.3. Pressure-time method

The pressure-time method, known as the Gibson method, was first introduced by Norman Gibson in 1923 [5]. This method measures the pressure rise during flow deceleration within a closed conduit, typically a penstock in hydropower power plants. This pressure transition is accompanied by a water hammer effect. The magnitude of the pressure rise is influenced by the speed of valve closure, the average velocity in the pipe and the pipe length. A rapid closure results in larger pressure amplitudes.

According to the IEC-60041 standard, the uncertainty of the pressure-time method is satisfactory, falling within the range $\pm$ (1.5-2.0)% [3]. In addition its practical application in hydropower, the pressure-time method is also potentially useful for flow measurement in various other applications.

As specified in IEC-60041, Eq. (1) enables estimation of the flow rate by integrating the measured differential pressure variation plus viscous pressure losses between two cross-

sections during the deceleration of a fluid mass within a straight pipe of constant cross-section.

$$Q = \frac{A_c}{\rho L} \int_0^{t_f} (\Delta p + \Delta p_f) \, dt + q \qquad\qquad \text{Eq. 1}$$

In Eq. (1), the variables Δp_f, Δp, L, A_c, ρ, Q, t_f, and q represent the pressure loss due to friction, differential pressure, the length between two cross-sections, cross-sectional area, fluid density, initial flow rate prior to valve movement, final limit of integration, and leakage flow rate after valve closure, respectively.

Figure 2 depicts a schematic of the measured differential pressure and pressure loss variation caused by friction in the pressure-time method. The area between the two curves (Δp and Δp_f) is proportional to the initial flow rate. In Eq. (1) the integration endpoint has to be estimated. The accuracy of the pressure-time method relies on the precise estimation of pressure loss, determination of the integration endpoint, and consideration of the uncertainties associated with the measured variables.
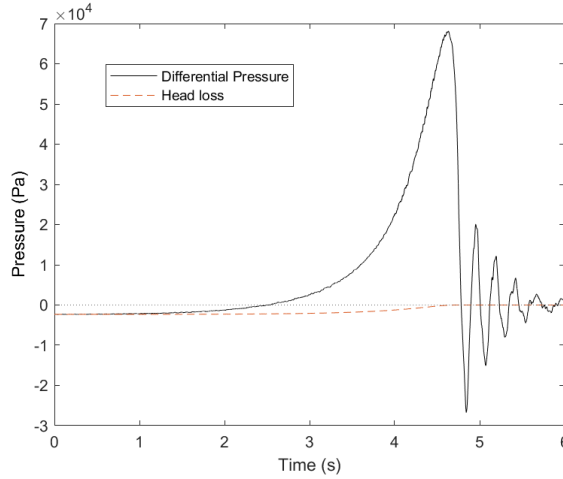
Figure 2 Example of differential pressure and pressure loss variation using the pressure-time method

To initiate the the pressure-time method, a linear flow rate profile is initially assumed as a preliminary estimation during the transient pressure period. The Constant coefficient of friction losses (K) is calculated from this initial flow rate. Subsequently, the flow rate is iteratively computed in a loop using Eq. (1). The pressure loss is updated after each iteration

based on the obtained flow rate. This iterative process continues until a convergence criterion is satisfied.

According to IEC-60041 guidelines, the conventional pressure-time method may not provide accurate flow rate measurements for low-head machines. The IEC-60041 standard specifies limitations for the pressure-time method. For instance, the distance between the two cross-sections should exceed 10 m. Additionally, the product of the measurement length (L) and average velocity in the section (U) should be more than 50 m²/s to ensure accurate measurements. A lower velocity and shorter distance than those stipulated in the IEC standard create a lower pressure loss and pressure rise for a given closure time. Therefore, the higher relative uncertainty of the measured differential pressure leads to higher measurement uncertainty in the estimated flow rate. The cross-sectional area between these sections must remain uniform without significant irregularities. Additionally, pressure taps should be positioned at least two diameters away from any irregularities in the penstock. This limitation can be attributed to the complexities caused by developing and non-uniform flow patterns within the short water passages characteristic of low-head machines.

1.4. Improvements in the pressure-time method

Numerous studies have been conducted to enhance the accuracy and broaden the application of the pressure-time method. The studies can be divided into two main groups. The first relates to improving the method's accuracy for the conditions cited in IEC-60041. The second extends the applicability of the pressure-time method beyond the scope of IEC-60041, such that the method can handle variations in the cross-section, bends, shorter lengths, and lower velocity.

In the standard pressure-time method, two crucial aspects affect the method's accuracy: determining the integration's endpoint and estimating the head loss attributable to friction. IEC-60041 provides specific guidelines for determining the integration endpoint. This method calculates the end time based on the free oscillation period and logarithmic damping after valve closure [3]. The second method, introduced by Adamkowski et al. [6,7], assumes a constant frequency and logarithmic fading ratio for the differential pressure oscillation following valve closure (Eq. (2)).

$$\Delta p(t) = B_0 e^{-ht} cos\ (\omega t) \qquad\qquad \text{Eq. 2}$$

The integration of Eq. (2) over time is set equal to zero in order to identify a suitable endpoint. The third method involves selecting endpoints close to the peaks and valleys [8]. The errors are minimised in proximity to these points. Additionally, filtering techniques can be used to accurately identify the peaks and valleys in noisy signals for precise estimation of the endpoints.

In addition to determining the endpoint, estimating the head loss due to friction is an essential aspect to consider in the pressure-time method. Based on IEC-60041 [3], the viscous pressure losses (ΔP_f) are traditionally assumed to be proportional to the square of the flow rate, as estimated by $\Delta P_f = KQ^2$. However, an alternative proposal suggests that the flow direction after valve closure influences the pressure loss and can be calculated as $\Delta P_f = KQ|Q|$, which is reported to reduce flow measurement errors [7]. To improve friction factor estimation in unsteady pressure-time methods, the method of characteristics was used in different studies [9–11]. Jonsson et al. [10] reported a decrease in error of up to 0.4% by use of an unsteady friction factor, which was due to a better estimation of pressure losses compared to the standard pressure-time method.

CFD provides invaluable insights into flow characteristics that are unattainable using experimental measurements alone. Numerous CFD investigations have studied the flow during the pressure-time method by investigating the friction models [12–15].

Several studies have explored the feasibility of extending the applicability of the pressure-time method beyond the limitations outlined in IEC-60041. For straight pipes of constant cross-section, acceptable measurement results were reported even for lengths as short as 3 m and $U \times L$ values lower than 10 m²/s [9,16]. Differential pressure sensors had a mean error of approximately 1% while use of absolute pressure sensors resulted in errors exceeding 2% [9,16]. This discrepancy can be attributed to the uncertainty associated with full-scale sensors.

To apply the pressure-time method to curved penstocks, Eq. (3) can be used instead of $C = \frac{L}{A_c}$. The results presented by Adamkowski et al. showed that the modified geometry factor changed the discharge error by around 0.45% [17].

$$C = \int_0^L dx/A_c. \qquad\qquad \text{Eq. 3}$$

Ramdal et al. [18] examined the impact of bends on the pressure-time method. They found that the presence of two 45° bends resulted in a flow rate underestimation of around 1%.

However, they found that a single 90° bend resulted in a more substantial underestimation of 8.5%.

Another limitation is a varying penstock cross-section. Equation (1) assumes a pipe with a constant cross-section and does not allow for dynamic pressure variation. However, in measurement sections where there is a variable cross-section or secondary flows exist, it is necessary to consider a new term to estimate the dynamic pressure variation. The energy equation incorporates the dynamic pressure variation in Eq. (4) to encompass this phenomenon.

$$Q = \frac{1}{\rho C} \int_0^t (\Delta P_f + \Delta P + \Delta P_d) dt \qquad \text{Eq. 4}$$

where ΔP_d is the dynamic pressure difference defined by Eq. (5).

$$\Delta P_d = \alpha_2 \frac{\rho Q^2}{2 A_2^2} - \alpha_1 \frac{\rho Q^2}{2 A_1^2} \qquad \text{Eq. 5}$$

For laminar flows, a constant value of 2 is commonly used as the kinetic energy correction factor. However, in steady and fully developed turbulent flow conditions, a suggested value of approximately 1.05 is used [19]. The lower value in turbulent flow is attributed to the flattening of the velocity profile across the section [20]. It is important to note that these kinetic energy correction factor values are only applicable to steady and fully developed flow conditions [19].

1.5. Aim of the thesis

The main aim of this thesis was to extend the pressure-time method to low-head machines by use of 3D CFD simulation. To achieve this aim, 3D CFD simulation was initially used to model fluid flow during application of the pressure-time method. The numerical model made it possible to examine viscous losses and wall shear stresses under developing and developed flow conditions (Paper A). Moreover, the water hammer phenomenon has also been studied in detail using 3D CFD (Paper B).

Subsequent to this, a specially designed laboratory setup was constructed to facilitate testing to study the pressure-time method applied under conditions beyond the recommendations given in IEC-60041. The method was applied to shorter pipe lengths and smaller values of $U \times L$, and to pipes with varying cross-section, as well as pipes containing one or more bends (Papers C and E).

In addition to the mentioned experiments, to improve and broaden the applicability of the traditional 1D pressure-time method, it was combined with 3D CFD analysis. A methodology is presented that uses 3D CFD to assess the sources of error in the pressure-time method in the presence of a reducer (Paper D) and a bend configuration (Paper E), thereby enhancing the accuracy of flow rate estimation.

2. Numerical Simulation

2.1. Geometry of Test Case (NTNU test rig)

The test case examined in this chapter is drawn from experimental measurements carried out by Sundstrom et al. [21]. The configuration featured a straight pipe with a constant internal diameter of 300 mm. Figure 3 is a schematic representation of the experimental setup used in the investigation. A differential pressure transducer was used to measure the pressure variation between two sections, located 11 and 15 m upstream of the valve. Additionally, a hot-film probe was used to measure the wall shear stress at the cross-sectional point 10 m upstream of the valve. During measurements, the flow rate was maintained at $Q = 0.169$ m^3/s, corresponding to a Reynolds number of 7×10^5. In the numerical analysis, a simplified straight pipe geometry was assumed and other components such as elbows, fittings, etc., were removed from the water hammer test rig. This assumption was reasonable because the measurement sections are sufficiently far from the bend in the test rig. The pipe's length is set to 36 m, aligning with the water hammer oscillation period derived from experimental observations, thus ensuring compatibility.
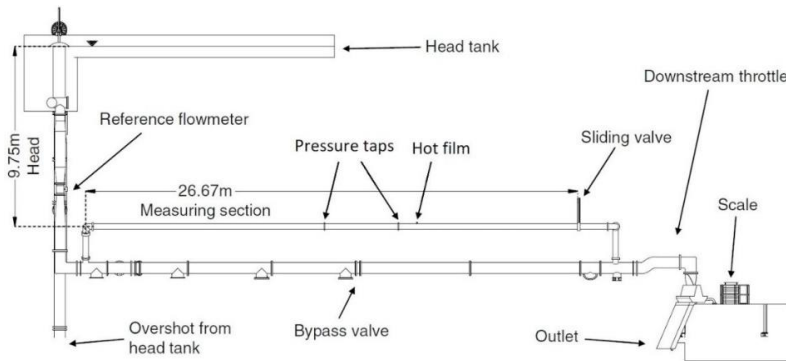
Figure 3 Schematic view of the water hammer test rig. Figure courtesy of Sundstrom et al. [21].

2.2. Flow and turbulence modelling

The equations governing the conservation of mass and momentum for an unsteady isothermal compressible turbulent flow can be expressed as follows:

$$\frac{\partial \rho}{\partial t} + \frac{\partial (\rho U_j)}{\partial x_j} = 0 \qquad\qquad \text{Eq. 6}$$

$$\frac{\partial (\rho U_i)}{\partial t} + \frac{\partial (\rho U_j U_i)}{\partial x_j} = -\frac{\partial p}{\partial x_i} + \frac{\partial}{\partial x_j}\left(\mu \frac{\partial U_i}{\partial x_j} - \rho \overline{u_i u_j}\right) \qquad\qquad \text{Eq. 7}$$

where, U_i, p, ρ, and μ correspond to the mean velocity, pressure, density, and dynamic viscosity, respectively. The turbulent shear stress term, $-\rho \overline{u_i u_j}$, is evaluated using the low Reynolds k-ω SST model proposed by Menter [22]. The k-ω SST model uses the omega formulation in the immediate vicinity of the wall and transitions into the k-ε formulation in regions situated further away from the wall [23]. This model has successfully been used in similar studies, see [12,14,24–26].

Density variation is modelled as a function of pressure variation. The fluid's bulk modulus of elasticity, denoted as K_f, is characterised by the relationship $p/d\rho = K_f/\rho$ [27], with temperature fluctuations disregarded. To accommodate the influence of the stainless steel piping on wave velocity, Eq. (8) is applied to adapt the fluid's modified bulk modulus, denoted as K_f'.

$$K_f' = K_f / (1 + \frac{K_f D}{eE})) \qquad\qquad \text{Eq. 8}$$

2.2.1. Numerical models

To mitigate the influence of the outlet boundary, an extension of 6 m was added downstream of the valve within the pipe, equivalent to $20 \times D$. During the steady-state simulation, the total pressure value at the inlet ($[P + \frac{1}{2}\rho U^2]_{inlet} = constant$) is adjusted to correspond to the flow rate observed in the experiment. Meanwhile, the atmospheric pressure ($P_{outlet} = p_{atm}$) is set as the outlet boundary condition. The boundary configuration and the geometry employed for the simulation are shown in Figure 4. A steady-state solution with a constant flow rate is adopted as the initial state of the transient simulation.
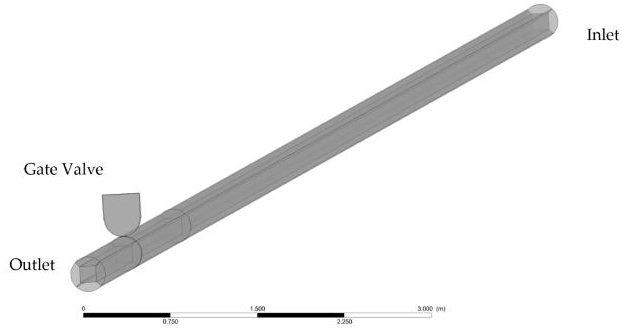
Figure 4 The boundary conditions and geometry used for the simulation.

2.3. Different methods for modelling valve closure

Three different methods were used to model the valve closure: dynamic mesh, mesh motion, and immersed solid. Ansys-Fluent was used to model valve closure using the dynamic mesh and sliding mesh methods while Ansys-CFX was used to model valve closure using the immersed solid method.

2.3.1. Immersed solid method

In the immersed solid method, the valve body is represented by the immersed solid domain, and the pipe represents the fluid domain, as shown in Figure 5. At each time step during the simulation, the method identifies the overlap region between the fluid domain and the immersed solid domain. In the fluid cells that intersect with the immersed solid cells, a source term is introduced into the momentum equation to ensure alignment between the fluid velocity and the solid velocity [28]. While this approach forces the fluid velocity to match the immersed solid velocity, it may not precisely capture the same physical phenomena. Specifically, the portion of the fluid domain overlapping with the immersed solid exhibits a downward velocity akin to the valve's motion, even though there should be no water present in this region. Furthermore, the estimation of the source term by the solver may introduce some potential leakage through the immersed solid [29].

20
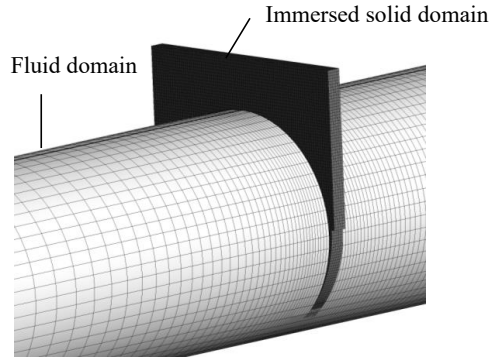
Figure 5 Overlap of the fluid zone with the immersed solid zone at time t=4s (close to the end of the valve closure) in the immersed solid method for modelling valve movement.

2.3.2. Dynamic mesh method

In the dynamic mesh method, the entire geometry is subdivided into three distinct domains: the pipe section preceding the valve, the region where the valve will be situated within the pipe, and the pipe section after the valve, as depicted in Figure 6. As the valve moves within the pipe, the upper segment of the valve domain moves downward, resulting in a reduction in the volume of the domain. This motion is executed perpendicularly to the boundary and necessitates the deformation and subsequent remeshing of the mesh structure. Interfaces are established to connect these domains, with the said interfaces regularly updated after each time step.
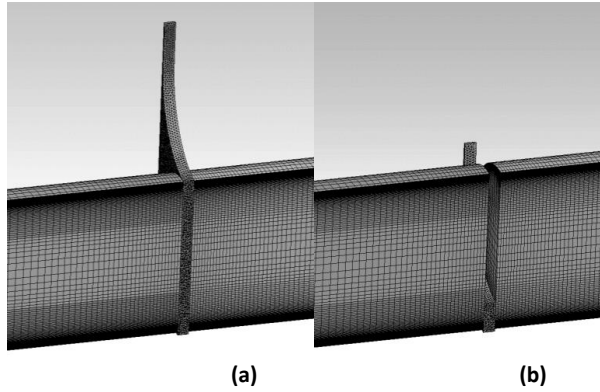
Figure 6 Dynamic mesh method grid cut in half: (a) before valve movement; (b) at t=4 just before the end of valve closure.

This re-meshing makes the simulation more time-consuming than the other two methods. At the end of the valve closure, the re-meshing space becomes smaller, increasing the risk of simulation divergence due to the difficulty in maintaining mesh quality. In an effort to address this issue, a lower under-relaxation factor value and a greater number of iterations are made at each time step, increasing the computational expense. Additionally, since the mesh undergoes updates after every time step, either through deformation or the introduction of a new mesh, data from the preceding time step must be interpolated, potentially introducing errors into the simulation results.

2.3.3. Sliding mesh method

In the sliding mesh method, the computational domain was structured similarly to the domain in the dynamic mesh approach, being divided into three sub-domains. Notably, the middle domain represented the location of the valve slides, eliminating the need for deformation or mesh adjustments. The remaining fluid zones remain stationary, while the mesh representing the volume occupied by the gate exhibits relative movement along the interface. Consequently, at each time step, the interface re-establishes connectivity for each zone.

In cases where boundaries do not overlap, wall boundaries are considered in order to take account of these situations. Since the mesh remains non-deformable, the downward motion of the valve zone extends to the base of the pipe, as illustrated in Figure 7. Consequently, there is no alignment with real conditions. This discrepancy could explain the preference for application of the dynamic mesh method in prior research concerning gate valve closure [4,10,11].

However, given the relatively small thickness of the valve body in comparison to the pipe's diameter ($0.06 \times D$), its potential impact on results is likely to be negligible when compared to the computational expense associated with more intricate methods such as dynamic mesh. It is worth noting that while Ansys-Fluent offers both axial and rotational mesh sliding capabilities, an axial movement capability is not available in Ansys-CFX.

(a)   (b)
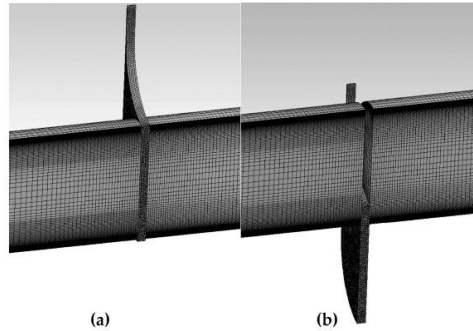
Figure 7 Sliding mesh method grid cut in half: (a) at t = 0 s before valve movement; (b) at t = 4 s just before the end of valve closure.

Due to simplification and its lower simulation cost, the immersed solid method for modelling valve closure during the pressure-time method presented in Paper A was considered in the first simulation attempt. Subsequently, the results of 3D CFD modelling with the three methods were compared as presented in Paper B. A detailed time step and mesh study has been conducted and is presented in papers A and B.

2.4. Simulation results with the immersed solid method

The transient outcomes for modelling valve closure with the immersed solid method are compared with experimental data, including the variation in differential pressure between two cross-sections and the wall shear stress. The variations in differential pressure between cross-sections located 11 and 15 m upstream of the valve have been used for validation of the CFD results obtained using the immersed solid method [12]. Figure 8 shows a comparison of experimental and numerical differential pressure data. The highest pressure peak, oscillation frequency, and post-valve closure amplitude exhibit strong alignment with the experimental data. However, the underlying causes of the deviation between the numerical simulation and experimental measurements remain unclear. Numerous factors may contribute to this variation. For instance, the immersed solid method may not model the exact physical

phenomena. Moreover, it should be noted that the geometry employed is not an exact replica of the physical test rig.
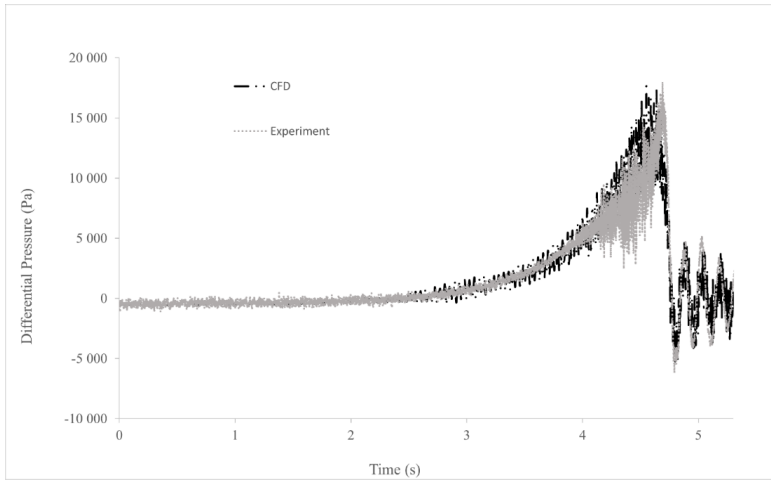
Figure 8 The differential pressure variation with time between two cross-sections 11 m and 15 m upstream of the valve

The developed model was used to investigate the endpoint of integration and friction models in the pressure-time method. Three methods for choosing the endpoint of integration were compared, and a new methodology was proposed. Moreover, different friction models in the pressure-time method were compared with the wall shear stress from CFD for developing and developed flows.

2.4.1. End time of integration

The obtained transient pressure data from CFD simulation has been used to check the sensitivity of the standard pressure-time method to the end point obtained by the IEC and Adamkowski methods [6]. The pressure-time method is applied to the differential pressure between two sections located 4 and 14 m upstream of the valve, and the constant friction factor assumption is applied to model the head loss. At these points, the flow is fully developed, and the distance between sections is 10 m, which complies with the limit in the IEC standard.

Figure 9 illustrates the variation of the differential pressure (left axis) and the associated error in the estimated flow rate (right axis) plotted against all times after valve closure. The differential pressure data exhibits high-frequency fluctuations, possibly stemming from the

numerical solver's instability when dealing with small time steps during simulation of the water hammer phenomenon during transients. The endpoints based on the IEC-60041 recommendation are indicated by vertical lines in Figure 9. These values closely align with those of the Adamkowski method, which is not explicitly presented.

The error relative to the reference value is computed using the formula $Error = \frac{Q_{PTM} - Q_{Exact}}{Q_{Exact}} \times 100$, which is based on the difference between the calculated flow rate derived from the pressure-time method Q_{PTM} and the exact flow rate Q_{Exact} obtained from numerical simulation.
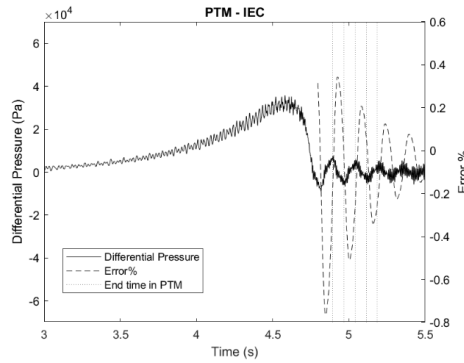
Figure 9 Differential pressure variation between two sections 4 and 14 m upstream of the valve and error in calculated flowrate based on IEC-60041

The estimated flow rate error in Figure 9 exhibits a 90° phase shift compared to the pressure oscillations. This implies that the minimum error corresponds closely to either the maximum or minimum pressure oscillation positions, similar to the findings in references [8,30]. The error associated with the pressure-time method's flow rate estimation ranges within ±1% as a function of the chosen endpoint. A slight change in the endpoint leads to a significant variation in the error. Thus, precise determination of the endpoint is essential.

Furthermore, the estimated error undergoes a more rapid decay than the pressure oscillation, diminishing after a few oscillations. It would be more accurate to select an endpoint when the variation in the estimated flow rate is damped. No specific guidance on this matter is provided in either the IEC-60041 or Adamkowski methods.

Also, finding the exact location of peaks and valleys in the differential pressure variation is challenging because of pressure data fluctuations. Moreover, even slight alterations in the endpoint selection can result in a substantial shift in the error value.

Based on the mentioned limitations, a methodology for determining the appropriate endpoint is proposed. This methodology estimates the flow rate function of various time intervals following valve closure as potential endpoints. Figure 10 illustrates the estimated flow rate functions of different endpoints, indicated by the dotted line. The damping ratio of these estimated flow rates exhibits temporal variability, making conventional curve-fitting approaches challenging. The selection of integration endpoints continues until the oscillations in the estimated flow rate are damped to a constant value. Subsequently, the oscillations in the estimated flow rates, derived from different endpoints, are mitigated through frequency-based filtering, as depicted by the solid line in Figure 10. By applying this approach to the differential pressure data, a flow rate of 0.1815 m³/s is determined, represented by the solid line (leading flow rate in Figure 10). This value exhibits a deviation of -0.081% from the reference flow rate, which is represented by the dash-dotted line. Notably, this deviation is lower than the conventional methods such as IEC or Adamowski. Therefore, this novel methodology offers a superior option, particularly for data affected by noise or pressure fluctuations.

However, it should be noted that this method may not be universally applicable, particularly in cases involving leakage or experimental measurements with extended integration times. It is important to anticipate additional errors when extending the integration time for measuring the differential pressure [31]. A thorough evaluation of the flow rate function at various endpoints is recommended, similar to the findings in Figure 10, followed by selection of an appropriate method based on the observed variation in the estimated flow rate function at different endpoints.
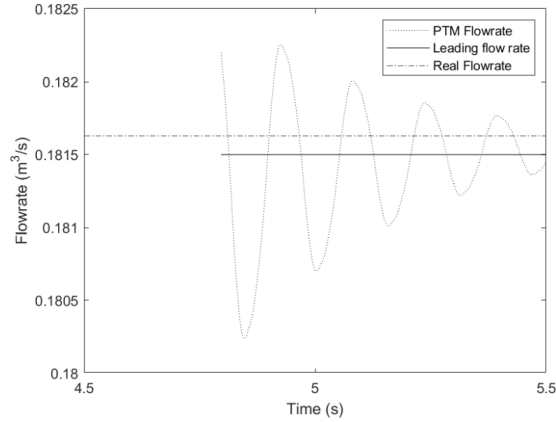
Figure 10 Flow rate variation based on different endpoints, actual and estimated flow rate based on the new methodology

2.4.2. Estimation of head loss due to friction

Pressure losses must be determined accurately in the pressure-time method. The pressure losses occurring prior to valve movement align with the measured differential pressure under steady-state conditions. To estimate pressure losses during and after valve movement, it is assumed that there is a constant friction factor sensitive to flow direction. This assumption of constancy in the friction factor is valid for large Reynolds numbers, where it can be reasonably consistent for a given level of roughness. However, the flow rate undergoes a continuous variation up to a quasi-null flow rate. Therefore, a quasi-steady friction factor could be a better assumption, as recommended in previous research [10,31].

Darcy's friction factor ($f = 64/Re$) is used for laminar flow conditions, while Haaland's equation (as presented in Eq. (9)) [32] is used for fully developed turbulent flow with negligible roughness. Towards the end of the closure process, the flow becomes unsteady, as demonstrated by Saemi et al. [12]. In such scenarios, employing an unsteady friction factor, such as the Brunone model (Eq. (10)) [33], is likely to offer a more representative characterisation of the flow behaviour, as substantiated by the findings of Jonsson et al. [34].

$$f = (-1.8log\,(6.9/Re))^{-2} \qquad\qquad \text{Eq. 9}$$

$$f = f_q + \frac{kD}{V|V|}(\frac{\partial U}{\partial t} - a\frac{\partial U}{\partial x}) \qquad\qquad \text{Eq. 10}$$

where f_q, U and k are the quasi-steady friction factor, axial velocity, and weighting coefficient. k is calculated based on Vardy's shear decay coefficient C^*, which is calculated

as $k = \sqrt{C^*}/2$ [33]. Vardy's shear decay coefficient is $C^* = 0.00476$ for laminar flow, calculated from Eq.11 for turbulent flow.

$$C^* = 7.41 \times ((Re)^{log\,(14.3/Re^{0.05})})^{-1}$$

Eq. 11

Three different assumptions for head loss estimation have been examined, and their impact on the accuracy of the pressure-time method was assessed. These assumptions typically assume fully developed flow conditions. However, in the case of low-head turbines, achievement of fully developed flow within the penstock is rare. The flow in the penstock continues to develop, leading to corresponding variations in the friction factor. In the existing configuration, a distance of 12 m is necessary to achieve fully developed flow, corresponding to a Reynolds number ($Re_L = \rho u L/\mu$) of 7×10^5 where L is the length of the pipe.

Moreover, it must be realised that the flow is not quasi-steady during the whole transient phase of the pressure-time method [24]. Equations derived from Haaland's and Brunone's assumptions, which are based on fully developed flow assumptions, are not accurate for developing regions where the friction factor is changing. This discrepancy creates a bias error when estimating pressure loss during the initial integration period in developing regions, thereby leading to an error in flow rate estimation. Consequently, the study suggests a correction factor for estimating the head loss in developing regions.

The constant friction factor correction, denoted as "CF", is defined by Eq. (12) and (13). This correction factor is determined from the ratio of the actual pressure loss (P_f) to the estimated pressure loss (P_D) assuming fully developed flow. The pressure loss (P_D) is computed using the equation $P_D = \frac{1}{2} \rho f \frac{L}{D} (\frac{Q}{A})^2$ [35], where f represents the friction factor derived from either a quasi-steady or unsteady flow assumption. Under steady-state conditions, the flow rate is denoted as Q_0, and the pressure losses due to friction (P_f) equate to the pressure drop ΔP_{St}, which can be determined through experimental measurement (CFD in this case) prior to valve movement.

$$f_{Developing} = CF f_{Developed}$$

Eq. 12

$$CF = \frac{P_f}{P_D} = \frac{\Delta P_{St}}{\frac{1}{2}\rho f(\frac{L}{D})(Q_0/A)^2}$$

Eq. 13

The assumption of a constant friction factor was examined in Paper (A).

To facilitate a comprehensive comparison between results obtained from developed and developing flow regions, two distinct computations were conducted. The initial computation used differential pressure data from sections representing a state of developed flow (4-14 m upstream of the valve), while the second computation employed differential pressure data from sections in which there was a developing flow regime (24-34 m upstream of the valve).

Table 2 provides an overview of flow rate errors estimated by the pressure-time method using differential pressure data from the developed region (4-14 m upstream of the valve) and the developing region (24-34 m upstream of the valve). These errors were computed relative to the reference flow obtained from the CFD simulation. Additionally, different friction factors were applied to assess the accuracy of each method when estimating head loss as part of the pressure-time method: Constant, Quasi-steady, Unsteady, Modified quasi-steady (adjusted by friction factor correction) and Modified unsteady (adjusted by friction factor correction).

The findings indicate that the quasi-steady and unsteady flow assumptions primarily give accurate results for the developed flow region. In contrast, the quasi-steady and unsteady flow assumptions applied to the developing flow region lead to higher levels of error. Implementing modified quasi-steady and unsteady friction factors notably enhances accuracy, particularly within developing flow regions.

Both quasi-steady and unsteady flow assumptions have comparable error values. The quasi-steady flow assumption remains valid except for the final stages of valve closure, where the flow approaches zero, resulting in similar pressure losses for both methods. In theory, the unsteady assumption offers a more precise tool for predicting pressure losses due to friction near and after valve closure [10]. However, in the developing flow region, the error associated with the quasi-steady assumption is nearly identical to that of the unsteady assumption, as can be seen in Table 2. The underlying reason for this remains unclear, but it is assumed to stem from potential inaccuracies and uncertainties in the CFD modelling process.

The constant value of the correction factor *CF* used in obtaining the results in Table 2, applied in both developing and developed flow regions, is presented in the same table. In the developed flow region, *CF* has a value of 0.993, while in the developing region, it equals 1.044. Notably, *CF* has a greater influence in the developing flow region, where it has a 4.4% deviation from the nominal value of 1, as opposed to the developed region's 0.7% deviation.

This highlights the fact that without this coefficient, the quasi-steady and unsteady frictional models would misrepresent losses in developing flow areas.

Table 2 Error of the pressure time method based on different friction models in both developed and developing flow regions, in %

Friction factor	Developed flow region (4–14 m upstream of the valve)	Developing flow region (24–34 m upstream of the valve)
Constant	-0.081%	-0.333%
Q-steady	0.154%	-1.223%
Modified Q-steady	0.067%	-0.099%
Unsteady	0.097%	-1.279%
Modified unsteady	0.028%	-0.1401%
CF value in case of using modified Q-steady or modified unsteady	0.993%	1.044%

The modified quasi-steady and modified unsteady models exhibit superior accuracy when compared to the constant friction factor model proposed in IEC standards. This conclusion is substantiated by the observed variations in wall shear stress and pressure losses across different models during application of the pressure-time method. Figure 11 shows the normalised head loss variation ($\frac{P_f}{4L} \times D$) with diverse friction models (steady, modified quasi-steady, and unsteady) together with the mean wall shear stress derived from CFD data between two cross-sections situated 34–24 m upstream of the valve, where the flow is still developing.

The figure demonstrates that use of a constant friction factor results in an underestimation of head loss values during the time interval $2 < t < 4.5$ s. This discrepancy arises from the fact that the friction factor depends on the Reynolds number. As per the Moody diagram, lower Reynolds numbers yield higher friction factor values. Consequently, the application of a constant friction factor results in a systematic underestimation of transient head loss for cases with lower Reynolds numbers.

This conclusion is further affirmed by the findings presented in Table 2, where the modified quasi-steady and unsteady friction factors consistently provide more accurate flow rate

estimations than the constant friction factors, even within the developed flow region. Notably, the disparity between the quasi-steady and unsteady flow models primarily manifests after valve closure, where the unsteady model takes account of transient terms, as outlined in Eq. (10).
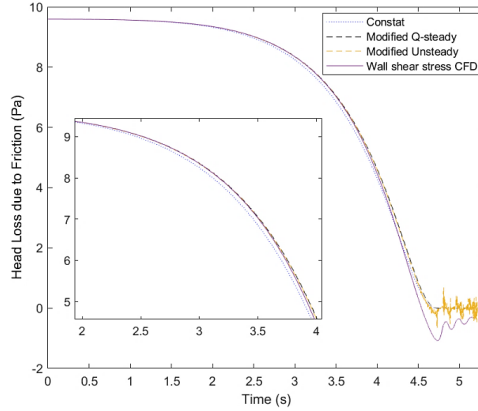
Figure 11 Variation of pressure loss during the pressure-time method with different friction models and wall shear stress calculated from CFD in the developed flow region

2.5. Comparison of CFD results for Different Methods of Valve Closure Modelling

The existing literature provides results of modelling fluid flow during rapid valve closure using different valve closure methods. These methods have been applied across various scenarios involving diverse types of valve closures. However, no previous research compares these approaches in terms of modelling precision and computational expense within the context of simulating valve closure during a water hammer transition. Additionally, it is also worth noting that a sliding mesh technique has not yet been investigated for modelling axial valve closure in this context. Therefore, three methods for modelling valve closure, including dynamic mesh, sliding mesh, and immersed solid methods, have been employed for the test case referred to in section 2.1.

The transient outcomes from three models, including the differential pressure between two cross-sections and the corresponding wall shear stress, are compared with experimental results. Figure 12 compares the variation in numerical differential pressure between two cross-sections, located 11 m and 15 m upstream of the valve, with the corresponding experimental data. Notably, the maximum peak differential pressure is lower for the

immersed solid method than for the experimental data. This discrepancy arises from a leakage flow rate after complete valve closure, equal to 0.06% of the initial flow rate. This leakage also occurs during valve movement, causing a delay in flow deceleration and subsequently affecting the momentum to pressure conversion, as evidenced by the slight delay in the pressure rise before t=4 s and underestimation of the maximum peak as apparent in Figure 12. Furthermore, the pressure oscillations after valve closure are also underestimated, possibly for similar reasons. Additionally, any potential errors in source term estimation may introduce fluctuations in the primary phenomenon, as can be seen in Figure 12. Moreover, in the immersed solid method, the maximum pressure peak occurs approximately 0.1 seconds earlier than in the experimental and other CFD results. This discrepancy may be attributed to the downward movement of water in the fluid zone overlapping with the immersed solid. Although a portion of the fluid domain overlapping the immersed solid exhibits a downward velocity similar to the gate, there should, in fact, be no water present.

Fluctuations are observed in differential pressure data obtained by the dynamic mesh method. The iterative process of mesh adjustment, extrapolation of data to accommodate the new mesh, and potential mesh distortion during smoothing can introduce errors in the simulation, potentially accounting for the observed instability. Comparatively, the re-meshing technique results in greater deviation from the experimental data compared to the results from the sliding mesh method, which uses a higher-quality mesh.

The sliding mesh method demonstrates better agreement in predicting the maximum pressure peak and oscillations after valve closure than the immersed solid and dynamic mesh methods. Additionally, the sliding mesh method also uses a higher-quality grid and forecasts pressure variations with lower fluctuations than the dynamic mesh. Moreover, this method demands fewer computational resources than the dynamic mesh.

It is worth noting that the results from both the sliding and dynamic mesh methods exhibit an overestimation of pressure oscillations post-valve closure when compared to the experimental data. This deviation may be attributed to the simplifications in the geometry and also the potential sensitivity of the experimental results to the tubing used in differential pressure measurements. Irregularities in the test rig and the presence of the tank may introduce a higher damping ratio compared to the geometry employed in the simulation.
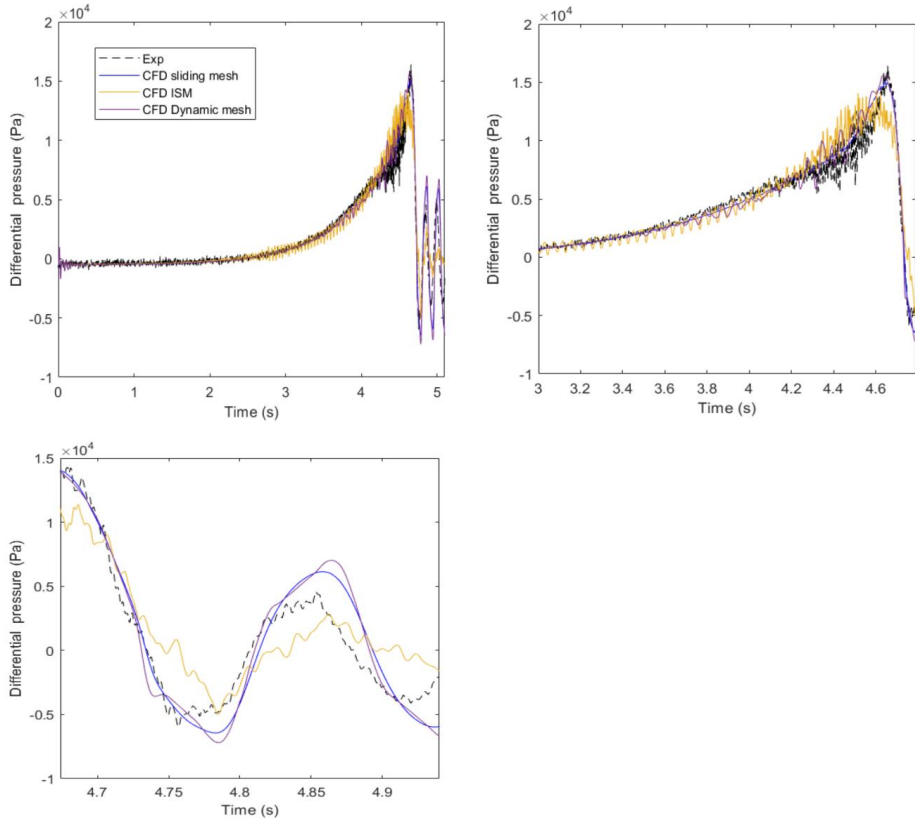
Figure 12 The variation of differential pressure with time during the valve closure between two cross-sections 11 m and 15 m upstream of the valve.

Figure 13 shows the normalised magnitude of the wall shear stress for the different methods employed. The results obtained using the sliding mesh and dynamic mesh methods show better agreement with the experimental normalised values than the immersed solid method. Conversely, the immersed solid method tends to overestimate wall shear stress between 3 and 4.6 seconds. This discrepancy could be attributed to a delayed reduction in flow rate and potential leakage associated with this method. Among the methods, the sliding mesh approach demonstrates the highest level of agreement in predicting wall shear stress during valve closure.

All methods tend to overestimate wall shear stress during the oscillations that follow valve closure. This deviation may be attributed to the uncertainty in the measurements and the presence of irregularities, such as elbows, reducers, and tanks in the test rig, which potentially

possess a higher damping ratio than the simplified geometry employed, which is just a single pipe.
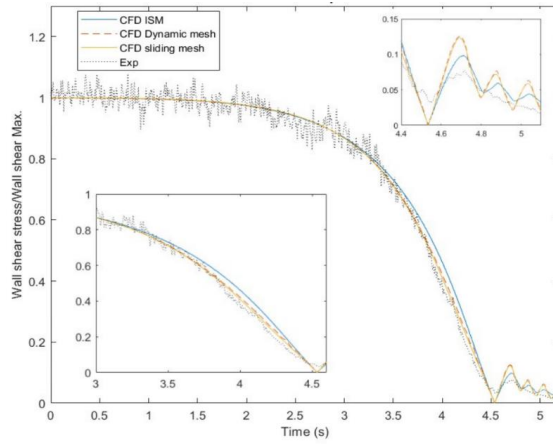
Figure 13 Time variation of the wall shear stress at cross-sections 10 m upstream of the valve

3. Experimental investigations

3.1. LTU test rig

To extend the boundaries of the IEC-60041 standard, a specialised testing apparatus was designed and manufactured at LTU. The primary focus of this test rig is to check the applicability of the pressure-time method beyond established limits, specifically targeting flow characteristics in scenarios similar to the low-head turbine condition. It is also potentially of use in other industrial flow measurement applications, such as developing flows, short measurement lengths, and flows in which irregularities such as bends and reducers are present.

A schematic representation of the experimental setup is presented in Figure 14. The arrangement consists of two tanks positioned at different elevations, interconnected by a stainless-steel pipeline with a roughness value of 0.0015 mm. Water flows in the pipeline between the two tanks due to gravity. The difference in elevation corresponds to a water column of 3.6 m which results in a maximum flow rate of 15 l/s. The Reynolds number associated with this experimental setup is approximately $Re \approx 2.4 \times 10^4$.

The experimental section encompasses a vertical pipe segment of 3.6 m in height, followed by a 3 m horizontal segment with both segments having a diameter of 150 mm. This horizontal section is followed by a standard concentric reducer (DN 150 to DN 65), 255 mm in length with a reducing angle of 9.46°. Downstream of the reducer, a 1 m pipe with a diameter of 65 mm is attached to a gate valve. The valve is operated by a servo motor, allowing it to close within 1 s.

The experimental setup encompasses a series of measurement sections, each serving a distinct purpose. A measurement section is positioned within the vertical pipe before the bend, labelled section VA. Downstream of the bend in the horizontal pipe, there are four additional measurement sections designated HA, HB, HC and HD upstream of the reducer, and one set of pressure taps downstream of the reducer, labelled as section HE, as shown in Figure 15. Four pressure taps are positioned around the pipe's circumference at intervals of 90° at each of the measurement cross-sections, as shown in Figure 16.

To minimise measurement uncertainty, differential sensors are favoured over absolute sensors, mainly due to their narrower measurement range [16]. The sensors are UNIK5000 differential pressure transducers, with a range of +/-35 kPa, and an accuracy of ±0.04% of the full scale. To ensure precise readings, calibration of the sensors is performed using a reference pressure calibrator, the Druck DPI 610 model.

The reference flow rate is measured using an Optiflux 2000F magnetic flowmeter, which has a high level of accuracy with a tolerance of ± 0.3%. A data acquisition system provided by National Instruments (NI-9239) is used for data recording. The system has a 24-bit data acquisition card operating at a sampling frequency of 4 kHz. The detailed systematic and random uncertainty calculation for the measurements is described in paper C.
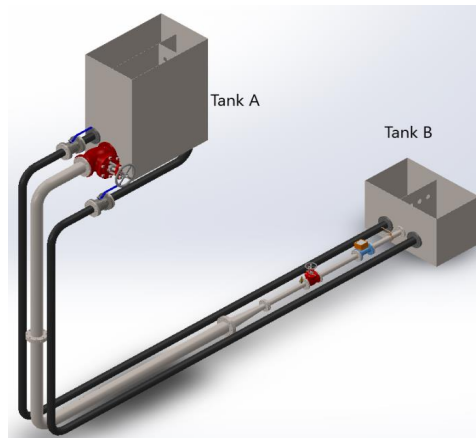
Figure 14 The schematic of the water hammer test rig
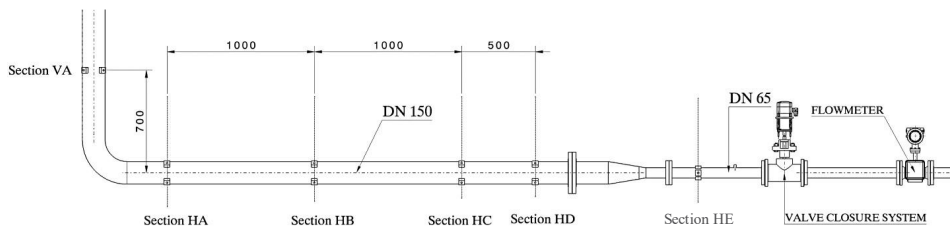
Figure 15 The location of the instrument
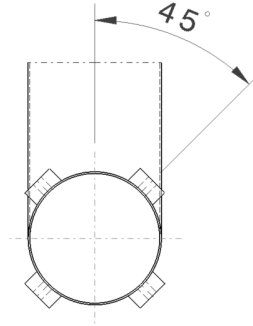
Figure 16 Pressure taps arrangement

Three sets of measurements were conducted. Initially, the measurements were made on a straight pipe with a shorter length and lower $U×L$ values than the values recommended in IEC-60041, while maintaining a constant cross-sectional area. In the second set of measurements, the pressure-time method was investigated in the presence of a reducer in a pipe exhibiting variable cross-section dimensions. The first two set conditions are listed in Table 3.

Finally, the third set of measurements investigates the impact of a 90° bend between two sections and the effect of locating the bend upstream of the measurement section, with a distance less than the IEC recommendation ($2×D$). The specification of the measurements, including the length between the sections and the distance to the bend upstream of the section, are listed in Table 4. Ten measurements were recorded for each case so that the random uncertainty of the measurement could be calculated.

Table 3 Experimental specification and results of the pressure-time method for different length

Test case	Measurement sections	Cross-section	Length (m)	U×L (m²/s)	L/D
Case 1	HB-HD	Constant	1.5	0.82	10
	HB-HC		1	0.54	6.7
	HC-HD		0.5	0.27	3.3
Case 2	HD-HE	Variable	1.275	0.69-3.67	8.5-19.6

Table 4 Description of the third set of measurements taken to study the effect of an upstream bend on flow measurements

Test case name	Inlet section	Outlet section	Elbow	Distance from the elbow to	
				Inlet section	Outlet section
VA-HA	VA	HA	yes	-	1.8 D
HA-HB	HA	HB	no	1.8 D	7.8 D
HB-HC	HB	HC	no	7.8 D	14.4 D
VA-HB	VA	HB	yes	-	7.8 D
HA-HC	HA	HC	no	7.8 D	14.4 D

3.2. Pressure-time method

To use Eq. (1) for flow rate estimation, it is necessary to determine the pressure loss resulting from friction. The constant friction factor that accounts for flow direction sensitivity ($\Delta P_f = KQ|Q|$) is used in the pressure-time method [7]. Within the framework of the pressure-time method, the K factor is derived from the initial flow rate observed prior to valve movement. At this point in time, the friction-induced pressure loss aligns with the measured differential pressure. Consequently, the friction factor can be determined using Eq. (14),

$$K = \frac{-\Delta P(t_0)}{Q(t_0)|Q(t_0)|}$$
Eq. 14

where, t_0 refers to steady-state conditions prior to valve movement. In the event of variation in the dynamic pressure, the constant friction factor K can be calculated by measurement prior to valve movement under steady-state conditions, when the integration of Eq. (4) is equal to zero as follows:

$$\Delta P(t_0) + \Delta P_d(t_0) + \Delta P_f(t_0) = 0$$
Eq. 15

Therefore, the constant friction factor K is calculated from the initial flow rate in accordance with Eq. (16).

$$K = \frac{-\Delta P(t_0) - \Delta P_d(t_0)}{Q(t_0)|Q(t_0)|}$$
Eq. 16

3.2.1. Pressure time method with quasi-steady assumption

As mentioned above, the friction factor is a function of the Reynolds number, as depicted in a Moody diagram. Consequently, relying on a constant friction factor may not yield accurate

results. In light of this, both the constant friction factor and quasi-steady assumption have been subjected to further investigation. The pressure loss predicted by the quasi-steady assumption at the time of initial valve movement has a bias error because the flow is not fully developed. A constant friction factor correction CF (introduced in Paper A) is used as follows in Eq. (17):

$$\Delta P_f(Q) = CF \cdot \Delta P_{f-QS}(Q) \qquad \text{Eq. 17}$$

where $\Delta P_{f-QS}(Q)$ is the pressure loss obtained assuming a quasi-steady and fully developed flow. For pipes with a constant cross-section, the estimation of pressure loss due to friction under the quasi-steady assumption employs the relationship $\Delta P_{f-QS} = \frac{1}{2} \rho f(\frac{L}{D})(Q/A)^2$. In the case of laminar flow, Darcy's friction factor ($f = 64/Re$) is applied, while for turbulent flow in the Reynolds number range of $3000 < Re < 10^5$, the Blasius law equation ($f = 0.316/Re^{0.25}$) is used due to its relative simplicity when compared to other models [35]. In scenarios where hydraulic turbines are subject to higher Reynolds numbers and greater roughness in the piping, an alternative friction model such as the Colebrook–White equation may be more suitable for field measurements.

For pipes with variable cross-sections, after integration to incorporate the reducer geometry, in cases of laminar flow, the pressure loss in the reducer is calculated as $\Delta P_{f-QS-Reducer} = \frac{128\mu Q}{3\pi} \frac{L}{D_1-D_2} \left(\frac{1}{(D_2)^3} - \frac{1}{(D_1)^3}\right)$, while for turbulent flow it is calculated as $\Delta P_{f-QS-Reducer} = 0.2411 \, \rho^{0.75} Q^{1.75} \mu^{0.25} \frac{L}{D_1-D_2} \times \frac{1}{3.75} \left(\frac{1}{(D_2)^{3.75}} - \frac{1}{(D_1)^{3.75}}\right)$. The detailed derivation of these equations is presented in the appendix. The pressure loss between sections HD and HE is the combination of different losses, including pipes of differing diameters and the reducer.

In a similar way, both constant and quasi-steady assumptions can be considered for the estimation of dynamic pressure variation. Various studies have reported a range of values from 1.03 to 1.11 for the kinetic energy correction factor α in turbulent flow [35,36]. The empirical equation (Eq. (18)), proposed by Szewczyk, provides a prediction for α in turbulent flow based on the Reynolds number [37].

$$\alpha = 1 + 0.101 \left(\frac{10}{\ln Re}\right)^6 - 0.107 \left(\frac{10}{\ln Re}\right)^4 + 0.113 \left(\frac{10}{\ln Re}\right)^2 \quad \text{Eq. 18}$$

Eq. (18) predicts more accurate values compared to predictions made using a constant value. The value indicated for α, may be affected by the intake geometry close to the measurement

section or possible secondary flows following valve closure, which should be considered before applying the pressure-time method.

Likewise, the geometry factor accounts for variations in different piping elements. For example, for measurements between sections HD and HE the cross-sectional area remains constant in both the straight pipes upstream and downstream of the reducer. Therefore, the geometry factor is determined by $C_1=L_1/A_1$ and $C_2=L_2/A_2$, where C_1 and C_2 represent the geometry factors for straight pipes upstream and downstream of the reducer. For the concentric reducer, the geometry factor is computed as $C_R = \frac{1}{4\pi}\frac{L_R}{D_1-D_2}(\frac{1}{D_2}-\frac{1}{D_1})$ (refer to the appendix for the derivation). The combined geometry factor between sections HD and HE encompasses all components, and is denoted as $C_T=C_1+C_2+C_R$.

3.3. Results

3.3.1. Effect of length

In Figure 17, the mean error and 95% confidence interval of the uncertainty of estimated flow rates obtained using the pressure-time method are depicted for measurements between sections HC - HD, HB - HC, and HB - HD to examine the effect of length on the accuracy of the pressure-time method. These measurements take into account the quasi-steady assumption with friction factor correction. It is worth noting that the results obtained using a constant friction factor, although not shown in Figure 17, yield an error of approximately 0.05% higher for all three cases. However, this discrepancy is considered negligible when compared to the overall measurement uncertainty. The applied friction factor correction falls within the range of approximately 1.18-1.25 between sections.

The length required to achieve fully developed pipe flow is given by $L= 1.359Re_D^{1/4} \times D$ [38], which in this context equals 3.5 m based on the Reynolds number. This condition is not met in the test rig. For the measurements, the pipe lengths considered are 0.5 m, 1 m, and 1.5 m. Notably, the shorter length of 0.5 m introduces a negative error with significantly higher uncertainty. This could be attributed to the lower initial differential pressure measurement before valve closure and a smaller pressure peak during valve closure.

Conversely, the mean error approaches zero for measurements between sections HB - HD and HB - HC, with uncertainties falling below 1%. This indicates that employing pipes with lengths of 1 m and 1.5 m, satisfying the criterion of $U \cdot L > 0.54$ m²/s, is acceptable according to the IEC-60041 standard.

Table 5 provides an overview of the experimental specifications, mean errors, and uncertainties with a 95% confidence level for all cases. The results reveal that a higher $U{\cdot}L$ product leads to a reduction in the random uncertainty of the measurements. This can be attributed to the increased differential pressure between sections, which results in more accurate measurements. Moreover, decreasing the length from 1.5 m (sections HB - HD) to 1.275 m (section HD - HE) and 1 m (sections HB - HC), induces a small negative error. Ref [39] reported a similar trend.
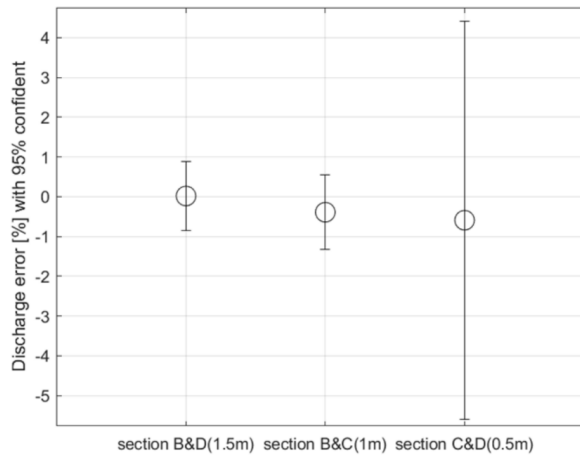
Figure 17 Flowrate error for 3 cases (sections HC-HD, sections HB-HC and sections HB-HD) with a quasi-steady flow assumption and friction factor coefficient. The bars represent the random uncertainty with 95 % confidence interval

Table 5 Experiment specification and results of the pressure-time method for different lengths

Measurement sections	Length (m)	U·L (m²/s)	Mean Error %	Random uncertainty with 95% confidence interval
HB-HD	1.5	0.82	0.02	0.86
HB-HC	1	0.54	-0.39	0.94
HC-HD	0.5	0.27	-0.59	5.01

3.3.2. Pressure time method for reducer

The presence of a reducer between sections HD - HE leads to a higher differential pressure, made up of both the pressure loss due to friction and dynamic pressure differences. Consequently, this increased measured pressure reduces the measurement uncertainty at this specific cross-section compared to all other measurements.

Figure 18 shows the mean estimated flow rate derived from the pressure-time method based on ten measurements conducted between sections HD - HE for the pipe with variable cross-section. Flow rate estimation was performed using both constant and quasi-steady state models for both the kinetic energy coefficient and the friction factor coefficient. The random uncertainty, determined with a 95% confidence level based on ten measurements, is equal to 0.34%. When employing the constant model for estimating both coefficients, the mean error is -0.83%. However, when applying the quasi-steady assumption to both coefficients, the mean error decreases to -0.42%. The friction factor correction for pressure loss is quantified as CF=1.78.

The impact of the quasi-steady assumption on head loss estimation is more pronounced in the flow rate estimation error, resulting in a 0.25% change. A similar value of 0.15% is obtained when applying the quasi-steady assumption to the kinetic energy coefficient. Introducing the quasi-steady assumption for both coefficients (while considering the friction factor correction) leads to higher coefficient values at lower Reynolds numbers. It is very important to mention this assumption is based on fully developed flow conditions; however, downstream of the reducer, the flow is still developing at section HE. Therefore, a more accurate estimation can be obtained using 3D CFD simulations.

The contributions of each term in Eq. (4) have been compared. The variation in differential pressure was approximately six times greater than the pressure loss due to the significant variation in cross-section within the reducer. Based on the definition $\Delta P_d = \alpha_2 \frac{\rho Q^2}{2A_2^2} - \alpha_1 \frac{\rho Q^2}{2A_1^2}$, it is evident that altering the diameter from DN150 to DN60 induces a substantial differential pressure compared to the pressure loss due to friction. This demonstrates the importance of accurately evaluating α at each section.

The total head loss encompasses losses occurring in the DN150 pipe, the reducer, and the DN65 pipe. Notably, the DN65 pipe accounts for approximately 60% of the total head loss, followed by the reducer at 38%, with the DN150 pipe contributing a mere 2%. This

distribution arises from the fact that pressure loss is proportional to the square of velocity, and velocity is inversely proportional to the square of diameter for a given flow rate. Consequently, pressure loss is inversely proportional to D^{-4}.

The reducer between sections HD - HE creates higher differential pressure which includes the pressure loss due to friction and the dynamic pressure differences. This higher measured pressure results in lower uncertainty for the referred to cross-section compared to all other measurements.
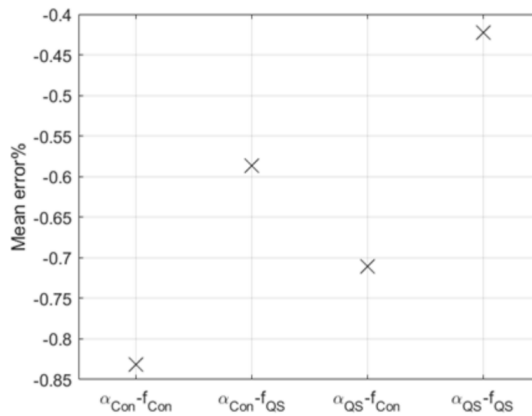
Figure 18 Flow rate error between section D & E with 4 assumptions: constant α & constant friction factor ($\alpha_{Con} - f_{Con}$), constant α & quasi-steady friction factor ($\alpha_{Con}- f_{QS}$), quasi-steady α & constant friction factor ($\alpha_{QS} - f_{Con}$), quasi-steady α & quasi-steady friction factor ($\alpha_{QS} - f_{QS}$)

3.3.3. Pressure time method for bends

Figure 19 illustrates the average deviation of measurements obtained using the standard pressure-time method in comparison to the reference flow rate, together with the associated random uncertainty with a 95% confidence level. This analysis considered five different measurement cases, each defined by the specifications outlined in Table 4. The differential pressure measurements are subject to a constant kinetic energy correction factor. Specifically, Figure 19-right presents results for two cases (VA-HA and VA-HB) where the bend is positioned between two measurement sections. Furthermore, Figure 19-left presents the results for three cases (HA-HB, HB-HC, and HA-HC) where the bend is located upstream of the initial measurement section.

After the bend, the flow profile causes non-uniform and developing flow characterised by Dean vortices. The differential pressure measured between the pressure taps deviates from the average pressure within the pipe sections, resulting in a deviation of the measured pressure relative to the mean pressure. For measurements in which the first section is located after the bend (HA-HB, HB-HC, and HA-HC), employing the standard pressure-time method yields a negative deviation when compared to the reference flow rate. Notably, measurements between sections HA-HB, where the first section is in closer proximity to the bend, exhibit a higher deviation of -0.74% compared to HB-HC, which displays a mean deviation of -0.39%. Moreover, measurements between sections HA-HC, with a length of 2 m, demonstrate a similar negative deviation of -0.55%, but with a lower random uncertainty (σ=0.3%). The reason for this is the higher measured differential pressure compared to the uncertainty of the sensor, which leads to lower random uncertainty. Conversely, in cases where the bend is positioned between two sections, the standard pressure-time method yields a positive deviation in flow rate measurement. Measurements between sections VA-HA, with a length of 1 m, exhibit a positive mean deviation of 1.30%, whereas measurements between sections VA-HB, with a length of 2 m, demonstrate a smaller positive mean deviation of 0.32%.

Among these measurements, the measurement between sections VA-HA has the highest random uncertainty (σ=0.78%), primarily because of transient secondary flows, which can vary between measurements. Notably, the measurements over a length of 1 m, particularly those between sections HB-HC (σ=0.47%), yield the lowest random uncertainty, because of the greater distance from the bend.
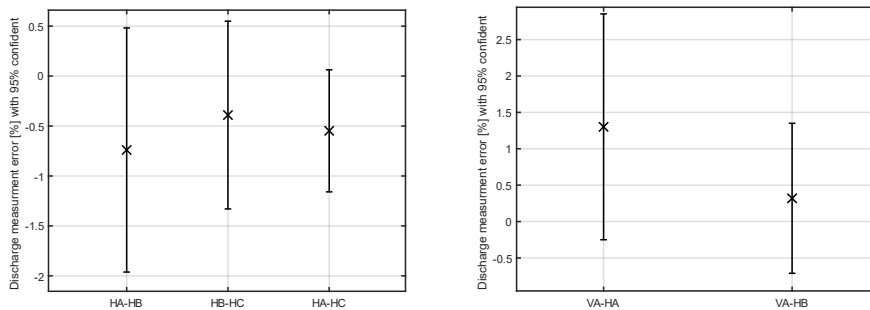
Figure 19 Mean deviation of the estimated flow rate compared to the reference flowmeter for 5 cases, left: between sections HA- HB, HB-HC and HA-HC, right: between sections VA-HA and VA-HB. The bars represent the random uncertainty with 95 % confidence interval.

# 4. Extension of the pressure time method by use of 3D CFD

The results discussed in the previous chapter were obtained assuming steady and fully developed flow. In unsteady conditions or in the developing flow region after the reducer or bend, the values of the kinetic energy correction factor and friction factor coefficients may vary. Moreover, bends can affect the symmetry of the pressure measurements. The skewed pressure profile observed in bends may lead to deviations in pressure measurement at pressure taps compared to the average pressure across the cross-section. The standard 1D pressure-time method assumes constant pressure over the cross-section. Therefore, the measured differential pressure from pressure taps in the pipe wall immediately after bends differs from the mean differential pressure in the pipe section, and boundary conditions may not be correct for the standard pressure-time method equation, leading to inaccurate flow rate estimation. Therefore, special consideration should be given to the impact of bend and reducer on pressure measurement accuracy and estimation of the kinetic energy correction factor. The hydrodynamic forces can be studied in detail using 3D CFD, and the distribution of variables in any section made available. Combining experimental data and 3D CFD analysis aims to enhance the traditional 1D pressure-time method and extend its applicability to more complex flow scenarios.

4.1. Numerical method

The primary objective of the 3D CFD simulation is to determine the velocity and pressure profile at the different sections of the test rig under similar flow conditions to those used in the experiment, which are subsequently employed to determine the mean pressure and kinetic energy correction factor which will be later used in the 1D pressure-time method. To do so, the time-varying flow rate obtained from the 1D pressure-time method is employed as an outlet boundary condition for the 3D CFD simulation. An iterative loop using the 1D pressure-time method and 3D CFD will be used to estimate the flow rate.

By applying the 1D pressure-time method with measured differential pressure, a transient flow rate, *Q (t)*, is determined. The transient flow rate obtained by applying the 1D pressure-

time method to the measured differential pressure between sections HD and HE is shown as an example in Figure 20. In this method, the friction coefficients and the kinetic energy correction factor are assumed to be constant. Subsequently, the obtained time-dependent flow rate is employed as a boundary condition for the 3D CFD simulation.
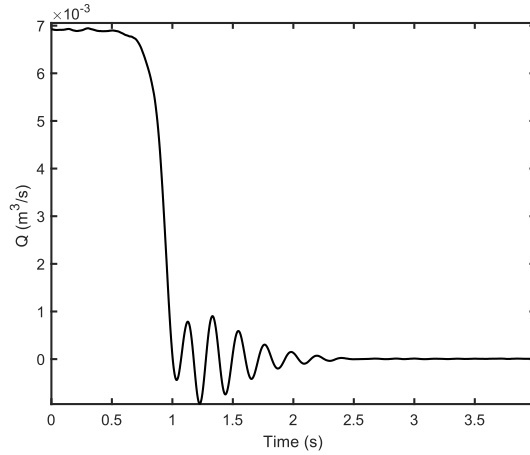
Figure 20 Transient flow rate estimated using the 1D pressure time method and experimental measurement.

To conduct the simulation, the continuity and momentum equations are used to simulate the incompressible isothermal fluid flow over time. To accurately simulate the oscillations following valve closure, it is imperative to account for compressibility effects [24]. However, the density variation is considered negligible because the water hammer wave associated with the valve closure is simulated using the 1D model, which is applied as the boundary condition. By applying both transient flow rate and density fluctuations, there will be interference between waves stemming from density changes and waves induced by variation of flowrates as the boundary condition.

To approximate the turbulent shear stress term, $-\rho\overline{u_i u_j}$, two turbulence models are employed: the standard k-ε [40] and the low Reynolds SST k-ω [41]. The standard k-ε model, with enhanced wall treatment, proves effective in predicting pressure loss in rough pipes [41]. This enhanced treatment employs a finely resolved mesh to accurately capture the laminar sub-layer and smoothly transition to the log-law function in the boundary layer, accounting for the impact of roughness on the flow [41]. To implement enhanced wall treatment, the dimensionless distance of the first grid (y^+) should be approximately unity [23].

The *SST k-ω* turbulence model is often considered a more accurate approach for predicting fluid flow in the near-wall region at low Reynolds numbers. This model uses the omega formulation near the wall and switches to the *k-ε* formulation further away from the wall, maintaining a y^+ value of approximately unity [23].

The simulation is conducted using ANSYS-Fluent, which solves the coupled finite volume equations of motion. The Semi-Implicit Method for Pressure-Linked Equations (SIMPLE) algorithm is used to compute the pressure field. The third-order monotonic upwind scheme discretises the nonlinear convective terms in all transport equations, in line with previous studies [14,24,26]. The first-order implicit scheme is employed to approximate the time derivative terms. Convergence is considered achieved when the root-mean-square (RMS) residual levels reach 10^{-5}.

A transient flow rate is imposed as a boundary condition at the outlet instead of explicitly modelling valve closure. This approach is preferred to avoid the additional computational time required for modelling valve closure. The entire upstream geometry of the valve is included in the simulation to capture the effects of developing flow. In Figure 21, the depicted flow domain used in the simulation is presented. The estimated transient flow rate *Q(t)* from the initial 1D pressure-time method shown in Figure 20 is applied as the outlet boundary (uniform profile) condition for the 3D CFD simulation. It could affect variable variations at measurement sections. However, the distance from the outlet boundary condition to the pressure measurement section is 10×*D*. A sensitivity analysis was conducted with an extended distance of 20×*D*, yielding identical results. Therefore, the assumption is made that the imposed uniform profile at the outlet does not significantly impact the results. It should be noted that there is a slight oscillation in the flow rate after valve closure, as depicted in Figure 20, which does not fully match physical reality given that the flow rate is zero at the valve location after valve closure.
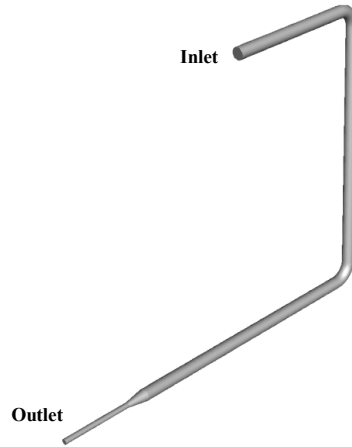
Figure 21   Fluid flow domain.

In the simulation, the total pressure is prescribed as the boundary condition at the inlet. Its value is adjusted in the steady-state simulation to reach the desired flow rate as in the experiment. A converged steady state with an initial mass flow outlet is set as the initial condition. Throughout the simulation, the value of the kinetic energy correction factor and variation of the pressure at sections is monitored. Figure 22 is a flowchart of the calculation.
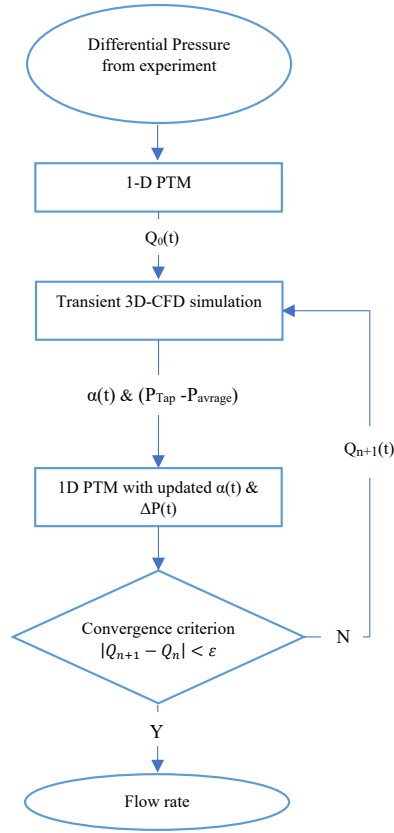
Figure 22 Proposed pressure-time methodology flowchart

A hexahedral mesh configuration is used to discretise the fluid domain, and is designed to accurately capture the flow up to a wall proximity of $y^+ \approx 1$, as shown in Figure 23. The mesh and time-step size analysis was presented in Paper D.

A mesh with 1.2 million elements, characterised by an average skewness of 0.08 and an average aspect ratio of 34, was selected for the simulation. The time step of 0.01 s was used for the simulation as an independent time step size. This time step of 0.01 seconds is 100 times greater than the time step employed for modelling valve closure in studies such as those cited in references [14,24,26], which highlights the increased speed of the presented 3D CFD simulation compared to other methods that incorporate valve closure modelling.
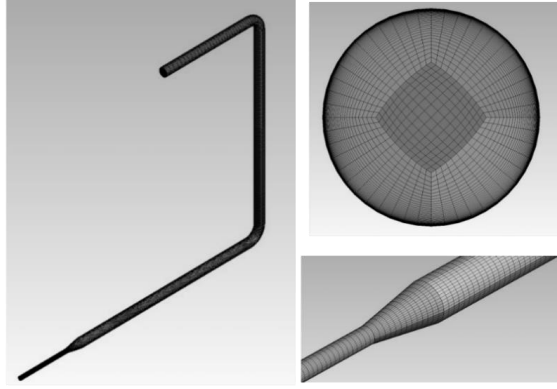
Figure 23 The generated grid of the pipe domain: complete domain, a pipe cross-section and a reducer.

4.2. Effect of variation in cross-section

Before integrating the 3D CFD results into the proposed method, it must first be validated. A selected sample of experimentally measured differential pressure between section HD-HE is used to compute the transient flow rate employing the 1D pressure-time method. This computed transient flow rate is then imposed as the outlet boundary condition for the subsequent 3D CFD simulation in accordance with the flowchart in Figure 22.

The differential pressures calculated from the 3D CFD simulations employing the k-ε and SST k-ω turbulence models are compared against the experimental differential pressure observed between sections HD and HE (Figure 24). Overall good agreement is observed between the calculated and experimental differential pressures, particularly using the k-ε turbulence model. It is worth noting that occasional spikes in the measurements are observed but these can be attributed to electrical noise in the data acquisition process. Discrepancies between the results of both turbulence models are noted just before starting closure of the valve, with the k-ε model exhibiting closer agreement with experimental data. This difference may arise from the k-ε model's capacity to predict velocity profiles near the wall in the complex flow region at the end of the reducer, where a significant portion of head loss occurs, approximately 60% of the total head loss (3.3.2). Although the literature suggests that the SST k-ω model is more accurate in predicting viscous losses [18], the standard k-ε model agrees better with the experimental data. Several sources of uncertainty in both modelling and experimentation make the comparison of the models challenging.

The geometrical parameters used in the CFD simulation, such as length, and roughness, may not perfectly replicate the physical model. Furthermore, due to challenges in precisely

modelling pipe junctions and fittings at a millimetre scale, these aspects have been omitted in the 3D CFD analysis for the sake of simplification. Additionally, any potential misalignment in the fittings could introduce additional pressure losses, which has not been considered. Moreover, the uncertainty in experimental measurements and potential deviations in flow rate measured by the 1D model (approximately -1% deviation) introduce further uncertainty.

Given these uncertainties, confidently establishing whether the k-ε model is more accurate thanthe SST k-ω model is challenging. Hence, both turbulence models are employed to estimate the kinetic energy correction factor using 3D CFD. The results indicate that the estimated flow rate exhibits variations of less than 0.1% when employing results from different turbulence models. This minimal difference in flow rate estimation, as per the presented methodology in Figure 22, highlights the independence of the kinetic energy correction factor estimation from the choice of turbulence model. However, as the outcome of the k-ε model was in closer agreement with the results, the final outcomes are presented exclusively using the k-ε turbulence model.

Two critical terms in Eq. (4) require estimation: the dynamic pressure difference variation and the pressure losses due to friction. These factors are comprehensively investigated using the obtained 3D CFD data, as detailed in the following sections.
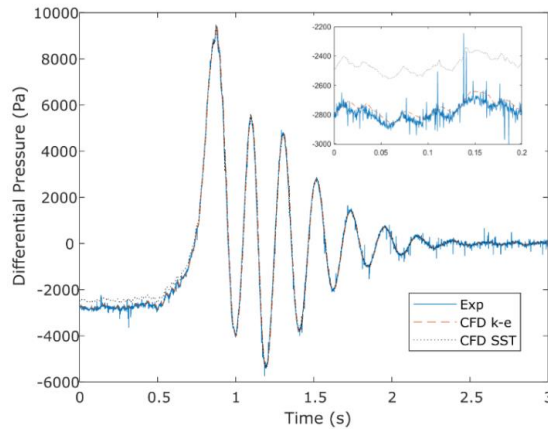

Figure 24 Comparison of differential pressure between sections HD - HE predicted by 3D CFD to the experiments.

The geometric transition from a 150 mm to a 60 mm diameter in the reducer induces a substantial dynamic pressure difference compared to the losses due to friction. To achieve an accurate estimation of the flow rate from Eq. (4), it is hypothesised that it is necessary to

estimate the variation of the kinetic energy correction factor at the two measurement cross-sections for the present case. Figure 25 depicts the variation of the kinetic energy correction factor at sections HD and HE during valve movement. In section HE, situated downstream of the reducer, the flow has a higher Reynolds number, resulting in a slightly smaller kinetic energy correction factor compared to section HD during the steady state prior to valve movement. Furthermore, a higher value of the kinetic energy correction factor is observed during flow deceleration and subsequent oscillation, as illustrated in Figure 25. This is related to a lower mean velocity present in the denominator of the kinetic energy correction factor during deceleration of the fluid.

The variation in the kinetic energy correction factor at the end of valve closure cannot be completely clarified because there is no such study in this region where the flow rate is close to zero, and in which the value of α has less influence on the accuracy of the method. Figure 26a presents the dynamic pressure variation between sections HD and HE, assuming a constant value for the kinetic energy correction factor alongside the variation predicted by 3D CFD. The predicted variation of the kinetic energy correction factor from 3D CFD, as shown in Figure 25, results in a higher dynamic pressure variation compared to the constant assumption depicted in Figure 26a. The discrepancies in estimated dynamic pressure between sections from the 3D CFD data and the constant assumption, as presented in Figure 26b, highlight the distinctions more prominently. Use of a constant friction factor and the underestimation of dynamic pressure variation diminishes the integral area in Eq. (4), which results in an underestimation of the flow rate.
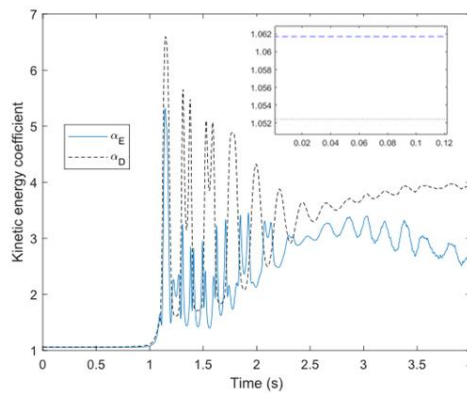
Figure 25 Variation of the kinetic energy correction factor at two sections HD (α_D) and HE (α_E)
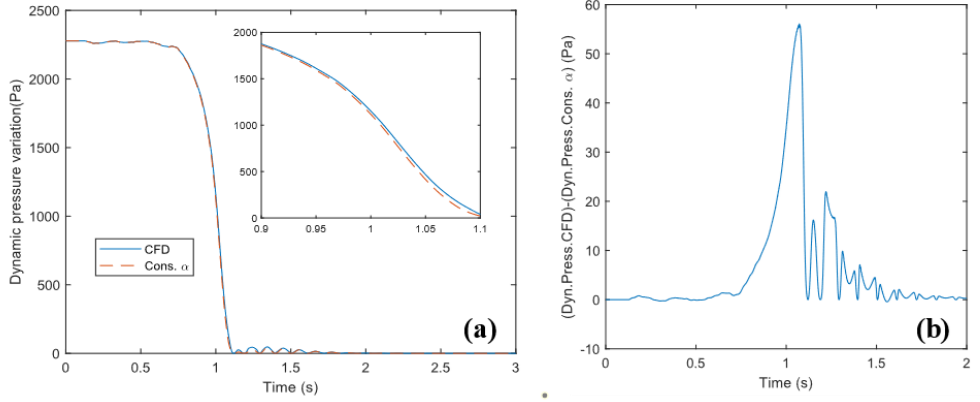
Figure 26 Variation of the dynamic pressure between sections HD - HE using a constant value for the kinetic energy correction factor and a value predicted by 3D CFD.

In a manner similar to the dynamic pressure, the variation in viscous losses as predicted by 3D CFD has been monitored and compared to the computed variation based on a constant friction factor given by $\Delta P_f(t) = KQ(t)|Q(t)|$ in the pressure-time method.

The friction-induced pressure losses from 3D CFD are approximated using the wall shear stress (τ_w). As the diameter changes along the reducer, these losses are derived by integration over the relevant wetted area, expressed as $\int_0^L \frac{4\tau_w}{D(z)} dz$. The calculated friction-based pressure losses from 3D CFD, accounting for both the magnitude of τ_w and considering only the axial component (z-axis), are compared with the losses obtained using a constant friction factor assumption in Eq. (15), as illustrated in Figure 27.

The magnitude of the wall shear stress does not exhibit negative values in its variations. The axial component of the wall shear stress fluctuates around zero and can thus become negative after the valve closure due to the creation of a recirculation zone upstream of the valve, as observed in a similar study by Saemi et al. [14]. Additionally, using the axial value of the wall shear stress from CFD is not accurate because the wall shear stress has a 3D structure in the presence of the reducer. The results demonstrate that the CFD simulation underestimates the pressure loss prior to valve movement. Furthermore, because the flow rate oscillates after valve closure, 3D CFD may overestimate the pressure loss after valve closure.

The estimation of wall shear stress using CFD introduces uncertainty related to the turbulence model and geometry simplification. Furthermore, the effect of roughness may not be accounted for in an actual penstock geometry. The mentioned uncertainties and

underestimation of viscous losses from 3D CFD results make it difficult to use 3D CFD results instead of an estimated pressure loss assuming a constant friction factor based on the experimental pressure measurements obtained prior to valve movement. Consequently, the presented methodology is limited to determining the time variation of the kinetic energy correction factor because of the inherent limitation of turbulence models in estimating friction losses accurately. Employing the 3D CFD pressure drop due to friction (both magnitude and axial value) significantly increases the deviation of the computed flow rate by up to 5%. A large part of this deviation arises from the pressure loss due to friction prior to valve movement. The 1D pressure-time method and the constant value of the friction factor coefficient are based on experimental measurements (prior to valve movement) and have a lower uncertainty than the viscous losses predicted by 3D CFD.

Hence, given the mentioned uncertainty regarding pressure losses with 3D CFD, the constant friction factor is considered appropriate for estimating pressure losses using the experimental data in Eq. (15) for calculation.
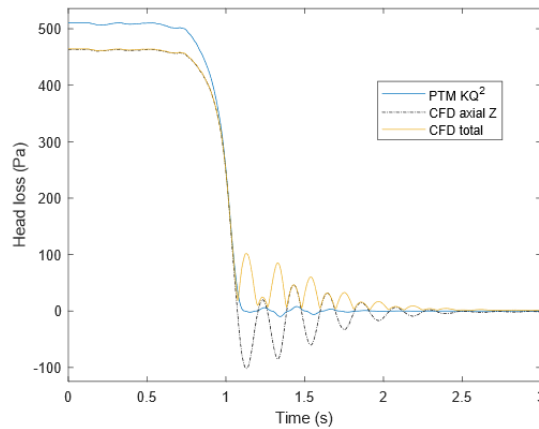
Figure 27 Variation of the pressure loss due to friction between sections HD - HE based on a constant friction factor and as predicted by 3D CFD (axial (z-axis) and magnitude of total wall shear stress)

To apply the presented methodology, the differential pressure data for one of the measurements with a result close to the mean deviation when compared to the reference flowmeter is now employed.

Then, employing the transient flow rate derived from the 1D pressure-time method and conducting a 3D CFD simulation, we include the kinetic energy correction factor obtained

from the 3D CFD in the 1D pressure-time method, as outlined in the flowchart of Figure 22. This process is iterated twice until it reaches the desired residual. The deviation of the estimated flow rate function of different endpoints is depicted in Figure 28, where discrepancies in the estimated flow rate remain below 0.02%, meeting the defined residual threshold. Remarkably, both the first and second iterations yield identical flow rates, indicating successful convergence after the initial iteration. After the first iteration, the mean deviation compared to the reference flow meter decreases from -0.9% (for constant coefficient) to less than ±0.1%.
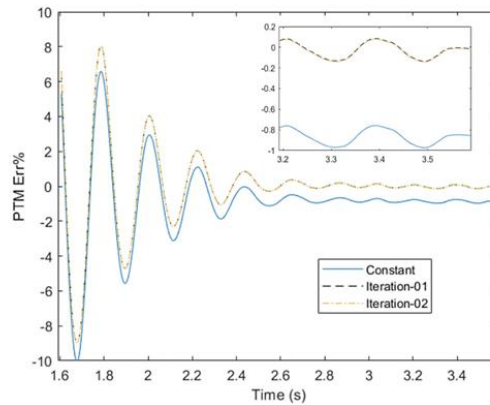
Figure 28 Variation of the deviation compared to the reference flow meter function of endpoints for the 1D pressure-time method for a constant value of α and 3D CFD for two iterations

To assess the sensitivity of our proposed methodology to different measurements, three out of the ten repeated measurement cases with the lower, higher and middle range of deviation compared to the reference flow meter were used. The deviation in flow rate estimation compared to the reference flow meter function of different endpoints, is illustrated in Figure 29. Similar patterns exist in the three cases. The mean deviation compared to the reference flow meter is changed using CFD data and has values between +0.8% and 0.9% for all cases. Consequently, the mean deviation in comparison to the reference flow meter undergoes a change from -0.83% to approximately ±0.1%. It is worth noting that the simulation efforts are focused on these three cases due to computational cost considerations, while other cases have not been included in this analysis.
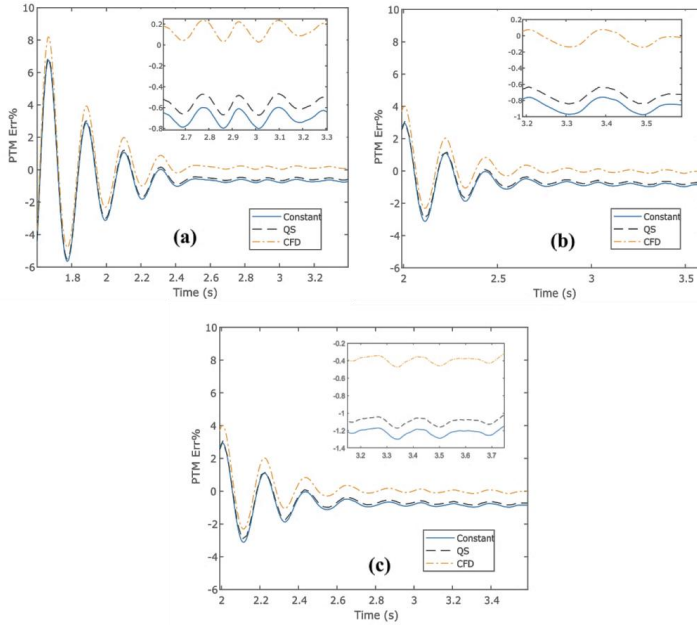
Figure 29 Improvement of flow rate deviation compared to the reference flow meter after applying the methodology for 3 cases at a) higher deviation bound, b) mean and c) lower deviation bound.

4.3. Effect of the bend

The methodology was implemented on an experimental measurement recorded between sections HA and HB. The transient flow rate, computed for a measurement sample between sections HA-HB using the 1D pressure-time method, was used as the boundary condition for the 3D CFD simulation. In this part of the thesis, simulation results from the SST $k\text{-}\omega$ turbulence model are presented because the $k\text{-}\varepsilon$ turbulence model predicts similar values. Figure 30 displays a comparison between the differential pressure obtained from the pressure taps between sections HA-HB using 3D CFD and the corresponding experimental measurement. The good agreement between the two sets of data, as seen in Figure 30, confirms the accuracy of the proposed approach. This demonstrates that 3D CFD can effectively replicate flow conditions similar to those observed in the considered experimental setups.
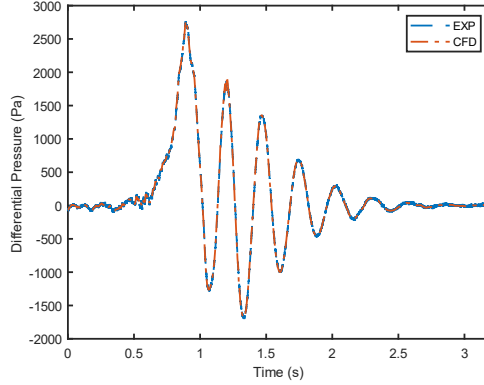
Figure 30 Experimental and 3D CFD numerical differential pressure between section HA-HB at the location of the pressure taps

After validation, 3D CFD is employed to check if there is any deviation in the measurement of the mean ΔP at the pressure taps compared to the mean pressure of the sections with the skewed pressure profile after the bend. Then, 3D CFD is used to estimate ΔP_d more accurately by using the predicted kinetic energy correction factor. For ΔP_f, the relationship $\Delta P_f = KQ|Q|$, which is sensitive to the flow direction is used, with K obtained from the experimental measurements. The reason for this approach is the difficulty 3D CFD has in accurately capturing the losses.

In Figure 31, the pressure distribution and surface streamlines are depicted at different sections downstream of the bend, as obtained from a steady-state simulation. The positioning of these sections is indicated relative to the diameter of the pipe. Note that the skewed pressure is clearly seen in both pressure contour and surface streamlines. It is apparent that the differential pressure readings from the pressure taps do not match the pipe section's average pressure. This discrepancy introduces a deviation in flow rate estimation when using the standard pressure-time method in comparison to the reference flow meter. Moreover, it can be seen that further downstream from the bend, the intensity of Dean vortices decreases.
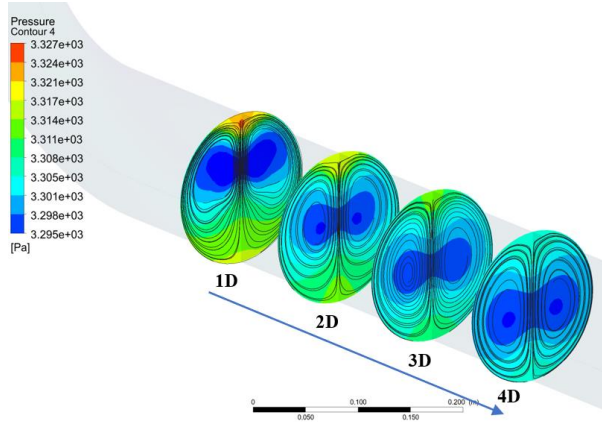
Figure 31 Pressure distribution and surface streamlines at different sections after the bend from steady-state simulation

The methodology is applied to the same set of experimental measurements taken between sections HA-HB. In the transient simulation, the pressure dynamics at four distinct sections (VA, HA, HB, and HC) are monitored. To estimate the deviation of the measured differential pressure from the pressure taps relative to the average pressure at the pipe sections, a normalised pressure deviation (ΔP_{Tap} -$\Delta P_{Average}$)/ $\Delta P_{Average}$ is introduced. Here, $\Delta P_{Average}$ is the average differential pressure between two sections derived from the 3D CFD analysis. On the other hand, ΔP_{Tap} represents the differential pressure between two sections, calculated by averaging the readings from the four pressure taps at each respective section, aligned with the locations of the experimental measurements.

The variation of the normalised pressure deviation throughout the pressure-time method is illustrated in Figure 32. Subsequently, the term $(\Delta P_{Tap} - \Delta P_{Average})_{CFD}$ is subtracted from the recorded differential data at the pressure taps to eliminate the deviation in the pressure measurement.
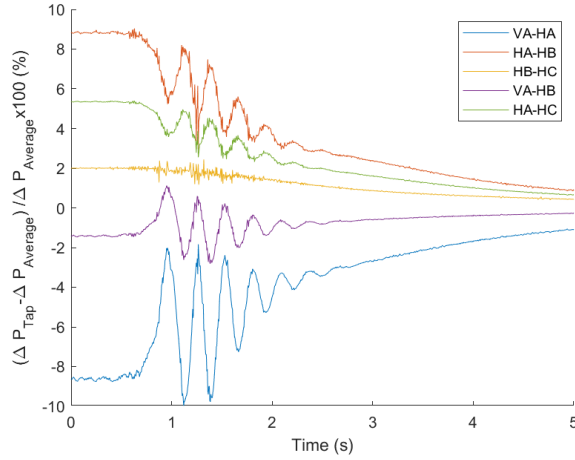
Figure 32 Normalised pressure measurement deviation at four sections

The CFD results, as depicted in Figure 32, offer valuable insights into the experimental discrepancies observed in the flow rate determined by the conventional 1D pressure-time method shown in Figure 19 (experimental results in 3.3.3). When the bend is positioned between two measurement sections, the pressure measurements tend to underestimate the differential pressure. For instance, in the case of the experimental measurements between sections VA and HA, the observed underestimation was up to -10%. Consequently, this leads to a lower value (with higher magnitude) for estimating the pressure loss prior to valve movement according to Eq. (16). Consequently, there is an overestimation of the area between the differential pressure and the pressure loss. This leads to an overestimation of the flow rate. The 3D CFD result provides a clear explanation for the overestimation of the flow rate in measurements between sections VA-HA and VA-HB as indicated in Figure 19-right (experimental results in 3.3.3).

Conversely, when the elbow is situated upstream of the initial measurement section, a positive deviation in pressure measurements at the taps is observed. Consequently, measurements for cases HA-HB, HB-HC, and HA-HC exhibit an overestimated differential pressure. This results in a larger value (with lower magnitude) being used to estimate the pressure loss. This leads to an underestimation of the area between the differential pressure and the pressure loss, consequently causing an underestimation of the flow rate. This is an explanation for the flow rate underestimation observed in the measurement displayed in Figure 19-left (experimental results in 3.3.3).

The case HB-HC has less deviation in estimating the average differential pressure from the experimental measurements at the pressure taps compared to the case HA-HB. This can be attributed to the increased distance from the bend. Consequently, there is a lower negative deviation in the flow rate estimation for this set of measurements. For the cases VA-HB and HA-HC, with larger distances (2m), the normalised deviation is smaller (Figure 32), resulting in a smaller mean deviation compared to the measurements of VA-HA and HA-HB when using the standard pressure-time method for flow rate determination.

The methodology is also employed in the experimental test case between HA-HB. Throughout the transient simulation, the variation in the kinetic energy coefficient and the deviation of pressure measurements at the pressure tap relative to the mean pressure are monitored. The obtained data is subsequently used to adjust the terms in the 1D pressure-time method.

The methodology is applied to a sample of each measurement group mentioned in Table 4, specifically those that closely align with the mean deviation The estimated flow rates are then compared to the reference flow rate function of different end points, presented in Figure 33. This analysis accounts for the impact of implementing the proposed methodology, which includes both a correction at the pressure taps and a dynamic pressure correction factor.

The results showed a consistent trend: the deviation in pressure measurements at the pressure taps has a more pronounced influence on the flow rate estimation compared to the dynamic pressure variation, across all cases.

Applying the methodology to measurements where the bend is situated upstream of the initial section increases the estimated flow rate. For instance, in the case of measurements between sections HA and HB, the deviation is changed by approximately +0.85%. In contrast, for measurements between sections HA and HC, characterised by a longer length, the methodology has a smaller effect, with a deviation change of around +0.3%. In the case of measurements between sections HB and HC, where the distance from the bend is greater, the alteration in deviation is even smaller, around +0.25%. This trend can be attributed to the observed deviation in pressure measurements at the pressure taps relative to the mean pressure, as shown in Figure 32.

Conversely, when applying the methodology to measurements where the bend is positioned between two sections, it results in a reduction in the estimated flow rate. For example, measurements between sections VA and HA, associated with the highest uncertainty in random measurements, exhibit a deviation change of approximately -1.8%. In contrast, for

measurements between sections HA and HC, characterised by a greater length, the impact is less pronounced, with a deviation change of around -0.6%.

In addition to this, the effect of considering the kinetic energy coefficient is smaller than the effect of pressure measurement at the location of the taps.
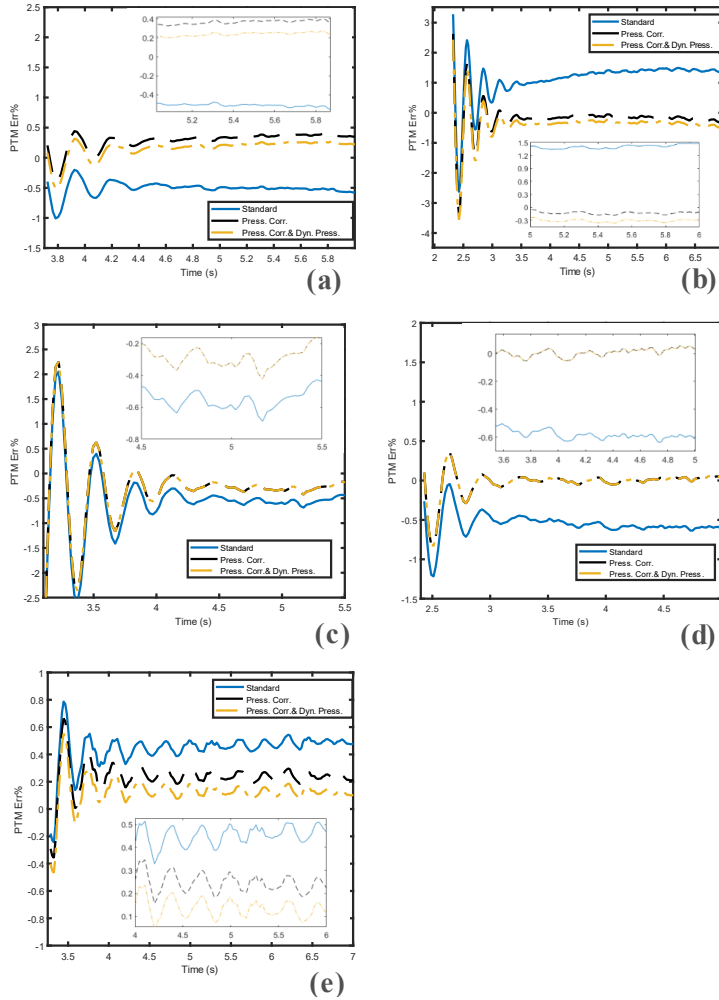
Figure 33 Flowrate deviation compared to the reference flow meter function of endpoint for all cases (a) HA-HB, (b) VA-HA, (c) HB-HC, (d) HA-HC, (e) VH-HB

The methodology outlined in Figure 22 was implemented across all cases detailed in Table 4. For each case, three measurements were selected based on their deviation from the reference flow rate as determined by the 1D pressure-time method. These measurements correspond to the greatest negative, least and greatest positive deviation from the mean.

Notably, it was observed that the degree of deviation change remained consistent among the three measurements within each case presented in Table 4. The flow rate discrepancy between different measurements within the same case fell below ±0.05%. Consequently, the mean deviation derived from the 1D pressure-time method was adjusted to the modified pressure-time method using the constant deviation change obtained from the three cases.

Figure 34 shows the mean deviation using the 1D PTM and modified PTM presented in the paper. The uncertainty with a 95% confidence level is only showed for the results based on standard PTM because the uncertainty is constant irrespective of whether standard or modified PTM is applied to the data.

The results reveal a notable reduction in mean deviation across all cases, specifically for four cases characterised by a random uncertainty of 0.6% or less. For the measurement cases characterised by a random uncertainty of 0.6% or less, including measurements between sections HB-HC, HA-HC, VA-HB, and HA-HB, the mean deviation, after employing the methodology, fell within the range of ±0.15%. This is within the systematic uncertainty of the reference flowmeter. In the case of measurements between sections VA-HB, characterised by the highest random uncertainty of 0.78% and an initial mean deviation of 1.3%, applying the methodology resulted in a mean deviation of -0.4%, falling within the range of random uncertainty of ten measurements between sections HA-HB. This variation can be attributed to secondary flows and transient vortex effects, which can vary under different circumstances, particularly when the length is 1 m.
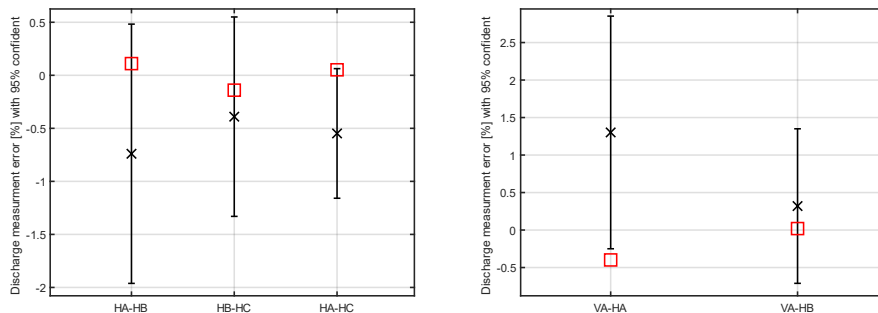
Figure 34 Flowrate deviation for all cases; × represents the mean deviation of the experimental measurement with 1D pressure-time method, □ represents the mean deviation with 3D CFD methodology. The bars represent the uncertainty with 95 % confidence interval based on the standard pressure-time method.

5. Conclusion and Future scope of research

This thesis studies the pressure-time method for application to low-head hydraulic turbines using a combination of numerical simulations and experimental techniques. The standard 1D pressure-time method is widely used for measuring flow rates in hydropower plants and stands out for its cost-effectiveness, straightforward installation, and minimal estimation error. Despite its numerous merits, the method does have its limitations, especially for low-head hydropower conditions. Moreover, before this study, no comprehensive investigation had been conducted on applying the pressure-time method under developing flow conditions. Consequently, the primary objectives of this thesis encompassed advancing the method beyond the constraints outlined in the IEC standard.

Initially, a 3D computational fluid dynamics analysis was used to explore the pressure-time method and the water hammer phenomenon. The numerical model was used to study different assumptions for the estimation of head losses and different methods for the calculation of the integration endpoint. Moreover, the transient simulation results obtained using three methods, dynamic mesh, sliding mesh, and immersed solid, are compared with the obtained experimental data.

A laboratory setup was specially designed and built for testing the pressure-time method based on IEC standards. The method was applied for smaller lengths and values of $U{\times}L$ outside the IEC-60041 recommendations in a pipe with constant cross-section. Furthermore, the pressure time method was studied with the existence of a reducer and bend. Finally, combining experimental data and 3D CFD analysis aims to enhance the traditional 1D PTM methodology and extend its applicability to more complex flow scenarios. This thesis presents a methodology that employs 3D CFD to quantify the various sources of error for measurements obtained with reducer and bend configurations, including deviations in pressure measurements at pressure taps and variation of the kinetic energy correction factor.

In accordance with the above explanations, the most important findings of the current thesis are discussed below:

5.1. Improvement of the pressure-time method with 3D CFD

- Calculating head loss using the modified quasi-steady and unsteady friction factors results in better agreement with the wall shear stress obtained from CFD than using a constant friction factor. Moreover, using the friction factor correction factor in both quasi-steady and unsteady friction factors further decreases error in developing and developed flow regions.

- The modified quasi-steady assumption is valid for most of the time in the pressure-time method except at the end of valve closure. At the end of and after valve closure, the flow is unsteady; however, this does not significantly affect the accuracy of the pressure-time method because the flow rate is close to zero.

- A novel approach was introduced, estimating flow rate using the pressure-time method function of different endpoint limits. By eliminating this oscillation, the flow rate could be estimated more accurately in comparison with other methods for estimating the integration endpoint.

- Among all the methods for modelling valve closure, the prediction of the sliding mesh method is closest to the experimental value. Moreover, the axial movement of the valve can be modelled by mesh movement without any mesh deformation.

5.2. Experimental results

- The results of measurements in the constant cross-section pipe show that the pipes with lengths of 1.5 m and 1 m have mean errors of 0.02% and -0.39% and uncertainty with a 95% confidence interval less than 1%, which shows that the pressure-time method is valid for $L>1$ m and $U{\cdot}L>0.54$ m^2/s.

- For measurements in the presence of a reducer, use of constant values for the friction factor and the kinetic energy coefficient lead to an underestimation of the dynamic pressure and consequently the flow rate.

- The random uncertainty in the measurements is found to increase as the measuring length and differential pressure decrease. Moreover, the presence of a reducer leads to higher measured differential pressure, resulting in lower uncertainty for variable cross-section measurements than for all other measurement scenarios.

- The results from the standard 1D PTM show that a bend between the measurement sections leads to an overestimation of the flow rate, while a bend upstream of the first measurement section leads to an underestimation of the flow rate.

5.3. Combination of 3D CFD and 1D pressure-time method

- The 1D pressure-time method was utilised to calculate the transient flow rate, which served as an outlet boundary condition for the subsequent 3D CFD simulation. The 3D CFD simulation was conducted to obtain detailed pressure and velocity profiles in different sections of the test rig under conditions similar to each experimental measurement. The obtained pressure and velocity profile information was then used to determine the deviation of the pressure measurement at pressure taps affected by the bend and the kinetic energy correction factor for each section, improving the accuracy of the 1D pressure-time method.
- The combination of 3D CFD and the 1D pressure-time method improves the accuracy of the pressure-time method. Applying the new methodology to measurements in the presence of a reducer (see 4.2) decreases the mean deviation compared to the reference flow meter from -0.83% to approximately 0%.
- Similarly, applying the referred to methodology for cases with the presence of a bend either between or in close proximity to a bend shows a significant improvement compared to the standard 1D pressure-time method (see 4.24.3). For cases with random uncertainty of 0.6% or less, the mean deviation after applying the methodology achieved a range of ±0.15%, which is within the range of the systematic uncertainty of the reference flow flowmeter. When the methodology was applied to measurements with the highest random uncertainty, the mean deviation was within the random uncertainty range.

5.4. Future scope of research

Despite its numerous merits, the presented methodology has only been tested in a laboratory test rig. It is essential to test the methodology on a larger scale test rig. Moreover, employing more sophisticated simulation approaches such as Large Eddy Simulation (LES) or Direct Numerical Simulation (DNS) could help in the use of CFD data to estimate viscous losses.

Furthermore, also recommended is the study of the impact of reducer shape variations, non-standard changes in diameter and bends with different angles, on fluid flow physics and the accuracy of flow rate estimations.

Reference

1.   *Renewable Energy, Our World in Data*; 2019;

2.   Halsnæs, K.; Bay, L.; Kaspersen, P.S.; Drews, M.; Larsen, M.A.D. Climate Services for Renewable Energy in the Nordic Electricity Market. *Climate 2021, Vol. 9, Page 46* **2021**, *9*, 46, doi:10.3390/CLI9030046.

3.   IEC 60041, I. Field Acceptance Tests to Determine the Hydraulic Performance of Hydraulic Turbines, Storage Pumps and Pump-Turbines. *International Standard* **1991**.

4.   Cervantes. M, Gunilla.A.Peter.K. and Sundström.J. *Flow Measurements in Low-Head Hydro Power Plants*; Stockholm, 2012;

5.   Gibson, N.R. Experience in the Use of the Gibson Method of Water Measurement for Efficiency Tests of Hydraulic Turbines. *Journal of Basic Engineering* **1959**, *81*, doi:10.1115/1.4008510.

6.   Adamkowski, A.; Janicki, W.; Krzemianowski, Z.; Lewandowski, M. Flow Rate Measurements in Hydropower Plants Using the Pressure-Time Method – Experiences and Improvements. *Flow Measurement and Instrumentation* **2019**, *68*, doi:10.1016/j.flowmeasinst.2019.101584.

7.   Adamkowski, A.; Janicki, W. Selected Problems in Calculation Procedures for the Gibson Discharge Measurement Method. In Proceedings of the GHEM; Roorkee, India, 2010.

8.   Ramdal, J.; Jonsson, P.P.; Dahlhaug, O.G.; Nielsen, T.K.; Cervantes, M. Uncertainties for Pressure-Time Efficiency Measurements. In Proceedings of the 8th International Conference on Hydraulic Efficiency Measurement ; IGHEM, 2010; pp. 64–72.

9.   Jonsson, P.P.; Cervantes, M.J.; Finnström, M. NUMERICAL INVESTIGATION OF THE GIBSON' S METHOD - EFFECTS OF CONNECTING TUBING -. *2nd IAHR International Meeting of the Workgroup on Cavitation and Dynamic Problems in Hydraulic Machinery and Systems* **2007**.

10.   Jonsson, P.P.; Ramdal, J.; Cervantes, M.J. Development of the Gibson Method-Unsteady Friction. *Flow Measurement and Instrumentation* **2012**, *23*, 19–25, doi:10.1016/j.flowmeasinst.2011.12.008.

11.   Dunca, G.; Iovanel, R.G.; Bucur, D.M.; Cervantes, M.J. On the Use of the Water Hammer Equations with Time Dependent Friction during a Valve Closure, for Discharge Estimation. *Journal of Applied Fluid Mechanics* **2016**, *9*, 2427–2434, doi:10.18869/acadpub.jafm.68.236.25332.

12.   Saemi, S.; Sundström, L.R.J.; Cervantes, M.J.; Raisee, M. Evaluation of Transient Effects in the Pressure-Time Method. *Flow Measurement and Instrumentation* **2019**, *68*, doi:10.1016/j.flowmeasinst.2019.101581.

13. Sundstrom, L.R.J.; Saemi, S.; Raisee, M.; Cervantes, M.J. Improved Frictional Modeling for the Pressure-Time Method. *Flow Measurement and Instrumentation* **2019**, *69*, doi:10.1016/j.flowmeasinst.2019.101604.

14. Saemi, S.; Raisee, M.; Cervantes, M.J.; Nourbakhsh, A. Numerical Investigation of the Pressure-Time Method Considering Pipe with Variable Cross Section. *Journal of Fluids Engineering, Transactions of the ASME* **2018**, *140*, doi:10.1115/1.4040718.

15. Adamkowski, A.; Janicki, W.; Lewandowski, M. Measurements of Discharge through a Pump-Turbine in Both Flow Directions Using Volumetric Gauging and Pressure-Time Methods. *Energies (Basel)* **2020**, *13*, doi:10.3390/en13184706.

16. Jonsson, P.P.; Ramdal, J.; Cervantes, M.J.; Getz, A. EXPERIMENTAL INVESTIGATION OF THE GIBSON'S METHOD OUTSIDE STANDARDS. In Proceedings of the 24th Symposium on Hydraulic Machinery and Systems; IAHR, 2009.

17. Adamkowski, A.; Krzemianowski, Z.; Janicki, W. Improved Discharge Measurement Using the Pressure-Time Method in a Hydropower Plant Curved Penstock. *J Eng Gas Turbine Power* **2009**, *131*, doi:10.1115/1.3078794.

18. Ramdal, J.; Jonsson, P.; Nielsen, T. Influence from Bends on a Pressure-Time Measurement. *IOP Conf Ser Earth Environ Sci* **2010**, *12*, 012078, doi:10.1088/1755-1315/12/1/012078.

19. Çengel, Y.A.; Cimbala, J.M. *Fluid Mechanics A Fundamental Approach*; 2018;

20. Franzini, J.B.; Finnemore, E.John.; Daugherty, R.L. (Robert L. Fluid Mechanics with Engineering Applications. **1997**, 807.

21. Sundstrom, L.R.J.; Cervantes, M.J. Transient Wall Shear Stress Measurements and Estimates at High Reynolds Numbers. *Flow Measurement and Instrumentation* **2017**, *58*, doi:10.1016/j.flowmeasinst.2017.10.003.

22. Menter, F.R. Two-Equation Eddy-Viscosity Turbulence Models for Engineering Applications. *AIAA J.* **1994**, *32 (8)*, 1598–1605.

23. ANSYS, Inc. *ANSYS Fluent User's Guide, Release 17.2.*; 2016;

24. Saemi, S.; Cervantes, M.J.; Raisee, M.; Nourbakhsh, A. Numerical Investigation of the Pressure-Time Method. *Flow Measurement and Instrumentation* **2017**, *55*, 44–58, doi:10.1016/j.flowmeasinst.2017.05.003.

25. Saemi, S.D.; Raisee, M.; Cervantes, M.J.; Nourbakhsh, A. Computation of Laminar and Turbulent Water Hammer Flows. In Proceedings of the 11th World Congress on Computational Mechanics (WCCM XI) 5th European Conference on Computational Mechanics (ECCM V) 6th European Conference on Computational Fluid Dynamics (ECFD VI); 2014.

26. Saeml, S.; Raisee, M.; Cervantes, M.J.; Nourbakhsh, A. Computation of Two- and Three-Dimensional Water Hammer Flows. *Journal of Hydraulic Research* **2019**, *57*, 386–404, doi:10.1080/00221686.2018.1459892.

27. Korteweg, D.J. Ueber Die Fortpflanzungsgeschwindigkeit Des Schalles in Elastischen Röhren. *Ann Phys* **1878**, *241*, doi:10.1002/andp.18782411206.

28. Yoon, Y.; Park, B.H.; Shim, J.; Han, Y.O.; Hong, B.J.; Yun, S.H. Numerical Simulation of Three-Dimensional External Gear Pump Using Immersed Solid Method. *Appl Therm Eng* **2017**, *118*, doi:10.1016/j.applthermaleng.2017.03.014.

29. Kalantar, M.; Jonsson, P.; Dunca, G.; Cervantes, M.J. Numerical Investigation of the Pressure-Time Method. *IOP Conf Ser Earth Environ Sci* **2022**, *1079*, 012075, doi:10.1088/1755-1315/1079/1/012075.

30. Mollicone, S. Latest Developments of the Pressure-Time Method. In Proceedings of the Proceedings of the American Power Conference, Chicago, USA; 1983.

31. Adamkowski, A.; Janicki, W.; Lewandowski, M.; Costa Bortoni, E. da Uncertainty Analysis of Liquid Flow Rate Measurement with the Pressure–Time Method. *Measurement (Lond)* **2021**, *185*, doi:10.1016/j.measurement.2021.109866.

32. Haaland, S.E. Simple and Explicit Formulas for the Friction Factor in Turbulent Pipe Flow. *Journal of Fluids Engineering, Transactions of the ASME* **1983**, *105*, doi:10.1115/1.3240948.

33. Brunone, B.; Golia, U.M.; Greco, M. Some Remarks on the Momentum Equation for Fast Transients. In Proceedings of the International Meeting on Hydraulic Transients with Water Column Separation (9th Round Table of the IAHR Group); 1991.

34. Bergant, A.; Ross Simpson, A.; Vìtkovsk[ygrave], J. Developments in Unsteady Pipe Flow Friction Modelling. *Journal of Hydraulic Research* **2001**, *39*, doi:10.1080/00221680109499828.

35. Yunus A. Çengel, J.M.; Cimbala *Fluid Mechanics: Fundamentals And Applications, Third Edition*; 2013; Vol. 53;.

36. White, F.M. *Fluid Mechanichs, 7th Edition*; 2011;

37. Teleszewski, T.J. Experimental Investigation of the Kinetic Energy Correction Factor in Pipe Flow. In Proceedings of the E3S Web of Conferences; 2018; Vol. 44.

38. Kakaç, S. (Sadık); Shah, R.K.; Aung, W. *Handbook of Single-Phase Convective Heat Transfer*; Wiley: New York, 1987; ISBN 9780471817024.

39. Jonsson, P.; Jonsson, P.P.; Ramdal, J.; Cervantes, M.J.; Dahlhaug, O.G.; Nielsen, T.K. *THE PRESSURE-TIME MEASUREMENTS PROJECT AT LTU AND NTNU*;

40. Barnett, M.; Lakshminarayana, B. Low-Reynolds-Number k-ε Model for Unsteady Turbulent Boundary-Layer Flows. *AIAA Journal* **1993**, *31*, doi:10.2514/3.11849.

41. Ahsan, M. Numerical Analysis of Friction Factor for a Fully Developed Turbulent Flow Using k–ε Turbulence Model with Enhanced Wall Treatment. *Beni Suef Univ J Basic Appl Sci* **2014**, *3*, 269–277, doi:10.1016/J.BJBAS.2014.12.001.

Appendix

The head loss is calculated based on the relationship $\Delta P_f = \frac{1}{2} \rho f(\frac{L}{D})(U)^2$. The reducer section is divided into n×dx parts, and for each part, the relation is equal to $\Delta P_{f-Reducer} = \int_0^L f \times \frac{1}{2} \frac{\rho}{D(x)} U^2 \, dx$

where f is the friction factor coefficient as a function of Reynolds number, determined as follows:

- Darcy's friction factor for laminar flow ($f = 64/Re$)
- Based on the Blasius law equation for turbulent flow $f = 0.316/Re^{0.25}$

Based on the concentric reducer geometry shown in Figure 35, the diameter is expressed as a function using the relationship $D(x) = \frac{D_2 - D_1}{L} x + D_1$ and the derivative of the diameter is equal to $dD = \frac{D_2 - D_1}{L} dx$.

For laminar flow, the equation is written as follows. Velocity U is replaced by flow rate divided by cross-section area (Q/A(x)).

$$\Delta P_{f-Reducer} = \int_0^L \frac{64\mu}{\rho U D(x)} \times \frac{1}{2} \frac{\rho}{D(x)} U^2 \, dx = \int_0^L \frac{64\mu}{D(x)} \times \frac{1}{2} \frac{1}{D(x)} (\frac{Q}{\frac{\pi}{4} D(x)^2}) \quad dx$$

$$= \frac{128\mu Q}{\pi} \int_0^L \frac{1}{D(x)^4} dx = \frac{128\mu Q}{\pi} \int_{D_1}^{D_2} \frac{1}{(D)^4} \frac{L}{D_2 - D_1} dD$$

$$= \frac{128\mu Q}{\pi} \frac{L}{D_1 - D_2} \times \frac{1}{3} (\frac{1}{(D_2)^3} - \frac{1}{(D_1)^3}) \qquad \text{App. (1)}$$

For turbulent flow, the equation is written as follows:

$$\Delta P_{f-Reducer} = \int_0^L 0.316 (\frac{\mu}{\rho U D(x)}))^{0.25} \times \frac{1}{2} \frac{\rho}{D(x)} U^2 \, dx$$

$$= \frac{0.316\rho}{2} \int_0^L (\frac{\mu}{\rho \frac{Q}{\frac{\pi}{4} D(x)^2} D(x)})^{0.25} \times \frac{1}{D(x)} (\frac{Q}{\frac{\pi}{4} D(x)^2})^2 \, dx$$

$$=\frac{0.316\rho^{0.75}\mu^{0.25}}{2}\int_0^L (\frac{\pi D(x)}{4Q})^{0.25} \times \frac{1}{D(x)}(\frac{4Q}{\pi D(x)^2})^2 dx$$

$$=\frac{16\times 0.316\rho^{0.75}\mu^{0.25}Q^{1.75}}{4^{0.25}\times 2\pi^{1.75}}\int_0^L \frac{1}{D(x)^{4.75}} dx$$

$$=0.2411\rho^{0.75}Q^{1.75}\mu^{0.25}\int_{D_1}^{D_2} \frac{1}{(D)^{4.75}}\frac{L}{D_2-D_1} dD$$

$$= 0,2411\rho^{0,75}Q^{1,75}\mu^{0,25}\frac{L}{D_1-D_2} \times \frac{1}{3,75}(\frac{1}{(D_2)^{3,75}} - \frac{1}{(D_1)^{3,75}}) \qquad \text{App. (2)}$$

Analogously to calculating the head loss, the reducer section is divided into n×dx parts, and the geometry factor is calculated as follows:

$$C = \int_0^L \frac{1}{A(x)} dx = \frac{4}{\pi}\int_0^L \frac{1}{(D)^2} dx = \frac{4}{\pi}\int_{D_1}^{D_2} \frac{1}{(D)^2}\frac{L}{D_2-D_1} dD$$

$$= \frac{1}{4\pi}\frac{L}{D_1-D_2}(\frac{1}{(D_2)} - \frac{1}{(D_1)}) \qquad \text{App. (3)}$$
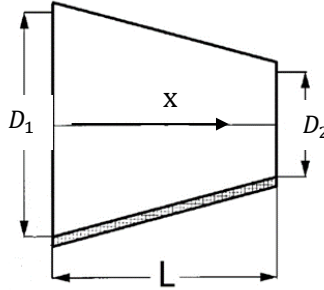
Figure 35 The concentric reducer geometry used for derivation of the equations

Department of Engineering Sciences and Mathematics
Division of Fluid and Experimental Mechanics

LULEÅ
UNIVERSITY
OF TECHNOLOGY